Coastal Engineering 188 (2024) 104452

Contents lists available at ScienceDirect

Coastal Engineering

journal homepage: www.elsevier.com/locate/coastaleng

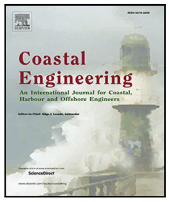

Hydrodynamic coupling of multi-fidelity solvers in REEF3D with application to ship-induced wave modelling

León-Carlos Dempwolff [a,*], Christian Windt [a], Hans Bihs [b], Gregor Melling [c], Ingrid Holzwarth [c], Nils Goseberg [a,d]

[a] Leichtweiß-Institute for Hydraulic Engineering and Water Resources, Technische Universität Braunschweig, Braunschweig 38106, Germany
[b] Norwegian University of Science and Technology (NTNU), Trondheim 7491, Norway
[c] Federal Waterways, Engineering and Research Institute (BAW), Hamburg 22559, Germany
[d] Coastal Research Center, Joint Research Facility of Leibniz Universität Hannover and Technische Universität Braunschweig, Hannover 30419, Germany

ARTICLE INFO

Keywords:
Groin overtopping
Long-period waves
Multi-scale modelling
Validation
Far-field wave
SWE-CFD coupling
Model interfaces

ABSTRACT

Ship-induced waves are an increasingly relevant hydrodynamic forcing factor in waterways travelled by large seagoing ships. The discrepancy between the small-scale wave-structure interaction near embankments and the larger-scale wave generation and propagation poses challenges for the prediction of ship-induced waves as a multi-scale problem. Therefore, a novel hydrodynamic coupling interface is presented that allows information transfer from the shallow-water-equation (SWE) solver REEF3D::SFLOW to the 3D-RANS-solver REEF3D::CFD. The implementation consists of a one-way coupling, where the solution from the SWE solver is imposed to one or multiple relaxation zones of the CFD solver. A series of verification cases shows that the implementation of the interface is accurate and only small deviations are introduced due to the 2D-3D dimensional mismatch of the numerical models involved. An application is presented, showing how the coupled SWE-CFD model can be employed to study ship-induced groin overtopping.

1. Introduction

Water waves are a design-relevant loading factor in coastal and ocean engineering applications, as they impose potentially large loads on the living and built environment in coastal and estuarine environments and can can trigger morphodynamic activity. The generation, propagation, and transformation of water waves when evolving through various water depths are characterized by a large range of time and length scales. On one side of the spectrum, are large-scale processes, that occur spatially on a kilometre scale and their effect – in the form of morphodynamic changes – on a weekly or yearly temporal scale. Recent examples of these spatio-temporal complex phenomena are e.g. on the long-term wave-induced morphological development of coastal stretches or islands (Schweiger et al., 2020; David and Schlurmann, 2020; Mehrtens et al., 2023). On the other end of this spectrum of scales are small-scale phenomena taking place on a centimetre and second scale; examples comprise processes pertaining to wave breaking (Elfrink and Baldock, 2002; Chen and Li, 2015; Aggarwal et al., 2020; Govindasamy et al., 2023) and fluid–structure interaction in close vicinity to engineered structures (e.g. Hattori et al., 1994; Chella et al., 2019; Krautwald et al., 2022; Gao et al., 2023) or the living environment (e.g. Kobayashi et al., 1993; Massel and Gourlay, 2000; Ma et al., 2013; Van Veelen et al., 2020; Keimer et al., 2021). Turbulence features may take place on an even smaller scale. This complex range of scales poses significant challenges to the numerical simulation of water waves, requiring to carefully balance computational accuracy and computational demand. The prediction of processes on a combined scale is particularly challenging, as high spatial resolution and large length scales oftentimes stand opposed. A variety of numerical methods, comprising nesting of domains with a different spatial resolution (Zhou et al., 2011), coupling of solvers describing varying dimensions (Mintgen and Manhart, 2018), or adaptive meshing (LeVeque et al., 2011), have therefore been presented in the past. All these works aim to shift the majority of the computational burden to the small-scale processes while maintaining sufficient accuracy for the large-scale processes.

Within the range of typical wave structure interaction processes in coastal and estuarine engineering applications, ship-induced waves acting on complex structural and bathymetric boundaries such as groins, natural embankments, or near-bank nature-based solutions, which include bio-engineered defence structures, are an increasingly important application where the range of scales can vary largely. A recent review by Dempwolff et al. (2022a) states that the hydrodynamic loads in

* Corresponding author.
E-mail address: l.dempwolff@tu-braunschweig.de (L. Dempwolff).

https://doi.org/10.1016/j.coastaleng.2023.104452
Received 6 September 2023; Received in revised form 24 November 2023; Accepted 27 December 2023
Available online 30 December 2023

Notation

ρ	Density.
ζ	Free surface elevation.
d	Still water depth.
g	Gravitational acceleration (9.81 m/s).
H	Wave height.
L	Wavelength.
l_{gen}	Length of the relaxation zone for wave generation.
P	Pressure.
p_d	Dynamic pressure.
q	Depth-averaged dynamic pressure.
T	Wave period.
t	Time.
U, V, W	Velocity components in x,y,z-direction.
u, v, w	Depth-averaged velocity components in x,y,z-direction.
x, y, z	Coordinates.

coastal areas induced by ships have increased largely in the past decades due to an intensification of large vessel traffic. In particular, when ships navigate in waterways limited in width and water depth, so-called confined channels, damaging long wave frequencies are generated through the ship's water displacement. While for most inland waterways established empirical equations provide sufficient guidance, these equations are not necessarily applicable to design situations where ships are navigating in more complex, estuarine environments (Almström and Larson, 2020), as often prevalent when sea ship access ports through coastal access routes (e.g. Muscalus and Haas, 2022). In such situations, ships can generate high-energy primary waves consisting of a bow wave, a drawdown, and a stern wave. These long-period waves can travel over large distances and are subject to shallow water wave deformation (shoaling, diffraction, refraction) (Rodin et al., 2015; Parnell et al., 2015) before they finally reach the embankments, where small-scale hydrodynamic phenomena, including fluid–structure interaction and wave breaking, take place. Hence, typical design problems where the prediction of ship-induced waves is required are the result of a process cascade consisting of the elements of ship wave (i) generation, (ii) propagation & transformation and (iii) interaction with bathymetric boundaries or structures.

Among the most common numerical approaches used to predict ship-induced waves are depth-averaged models, such as Boussinesq- (e.g. David et al., 2017; Forlini et al., 2021; Samaras and Karambas, 2021) or SWE-models (e.g. Almström et al., 2021; Dempwolff et al., 2022c). These models are generally able to simulate the generation of ship-induced primary waves via a moving surface pressure term (Bayraktar Ersan and Beji, 2013) and they can also model wave propagation over large distances including shallow water deformation effects. However, for the simulation of wave interaction processes in the vicinity of embankments (iii), the underlying assumptions of limited vertical accelerations in the flow fields and the absence of stratified flow components usually prohibit the application of depth-averaged models. For the simulation of near-bank small-scale processes, high-fidelity models, such as Reynolds-averaged Navier-Stokes equations (RANSE)—CFD, are therefore usually required, as these are capable of modelling depth-varying velocity components, breaking waves, and fluid–structure interaction in greater detail (Fleit et al., 2016, 2019). Despite the ongoing development of increasingly powerful computation hardware, three-dimensional (3D) high-fidelity modelling – even though usually employing parametric approximation for very small turbulent features through turbulence models – remains challenging for many applications of ship wave prediction, due to the long computation run time required to solve all non-linearities of common problem statements in space and time. Therefore, applications of RANSE-CFD models in the field of ship waves are commonly restricted to the relatively simple geometries of artificial or channelized natural waterways, which typically only require comparatively small numerical domains (e.g. Terziev et al., 2018; Du et al., 2020; Kochanowski and Kastens, 2022)

For other applications of coastal engineering, apart from ship wave prediction, coupling strategies between different numerical solvers have gained popularity in past years to overcome the limitations of the individual approaches of high-fidelity modelling and mid-to-low fidelity modelling. A number of interfaces have been developed, each aiming at balancing speed and accuracy for specific purposes. The suggested models comprise the coupling of 2D to 3D high fidelity CFD domains (Di Paolo et al., 2021a,b), the coupling of a spectral model to a phase-averaged model (Umesh and Behera, 2021), the coupling of potential flow theory-based models to RANSE models (Biausser et al., 2004; Paulsen et al., 2014; Vukčević et al., 2016; Choi, 2019; Wang et al., 2022), and the bi-directional coupling of a RANSE-model to a SWE model (Mintgen and Manhart, 2018). Yet, these model interfaces have not found application in the prediction of ship-induced loads.

To the authors' knowledge, the only documented multi-scale modelling approach to predict ship-induced waves was presented by Bellafiore et al. (2018). This approach is applied to the Venice-Lagoon, where the navigation channel is surrounded by tidal flats. In their work, a coupling strategy is presented, where the initial primary wave height is calculated using a RANSE-CFD tool, which is then used to model the further wave propagation over the adjacent shallow water areas with a SWE-solver. The work provides valuable insight into the nonlinearities during the propagation of ship-induced depression waves. However, the coupling approach suggested by Bellafiore et al. (2018) does not account for complex fluid–structure interaction near complex bathymetric boundaries, which would be required as the important third component (iii) to represent the whole process cascade required to predict ship-induced loads. One suitable simulation approach to model the expected processes in this region would be the application of a RANSE-CFD tool in this near-bank area.

The bi-directional coupling interface suggested by Mintgen and Manhart (2018) comprises such an interface between an in-house SWE-model and the RANSE-CFD solver OpenFOAM. The presented approach uses a combination of Dirichlet and Neumann boundaries to impose the water level and the respective flow velocities. As the authors aim for an application of their method in hydraulic engineering, a fully developed logarithmic velocity profile is assumed when imposing the solution of the depth-averaged solver to the 3D solver. No implementation of any means to represent ships in the shallow water equation solver is reported. Hence, the important process of ship wave generation (i) cannot be represented in the modelling approach, rendering the current version unsuitable for predicting ship-induced loads. In order to complement existing tools to predict ship-induced loads, a novel modelling tool is therefore required that allows a holistic simulation of the threefold process cascade of ship wave-induced loads. The present work therefore uses the REEF3D hydrodynamic modelling toolbox (Bihs et al., 2016; Wang et al., 2020a), as it includes solvers for fast, computationally efficient large-scale and computationally-expensive, high-fidelity applications. The non-hydrostatic shallow water equation solver REEF3D::SFLOW (Wang et al., 2020b) is able to simulate ship wave generation (i) and propagation (ii), in particular the often particularly damaging primary wave component (Dempwolff et al., 2022b,c). The high-fidelity RANSE-based CFD solver REEF3D::CFD (Bihs et al., 2016) has been successfully applied to various hydrodynamic applications (e.g. Aggarwal et al., 2020; Kamath et al., 2022; Martin et al., 2020, 2021), including ship-wave interaction with complex bathymetries (Fleit et al., 2016, 2019; Dempwolff et al., 2022c) (iii). Given these features, REEF3D provides the necessary prerequisites to develop a coupling interface to extend the suite of multi-scale engineering tools,

able to simulate the entire process cascade from ship wave generation (i), wave propagation & transformation (ii) with REEF3D::SFLOW, and wave interaction with embankments (iii) with REEF3D::CFD. The fact that the individual solvers are part of a modelling toolbox, has the additional benefit of a coherent workflow in pre-and post-processing.

To that end, this paper presents a novel coupling interface that was developed to obtain a prognostic tool for ship-induced waves near complex bathymetries, an approach that has not been reported in the pertinent literature. In order to establish the required confidence in the model's prognostic abilities for complex hydrodynamic phenomena, this study involves testing the new model coupling against a series of verification and validation benchmark sets to examine the performance in terms of wave kinematics. The specific objectives of the given study are threefold:

- To verify and validate a novel coupling interface between the SWE solver REEF3D::SFLOW and the RANSE solver REEF3D::CFD.
- To understand and analyse the effect of the dimensional mismatch between the 2D-input variables from the SWE-solver on the 3D-results obtained from the CFD-solver.
- To examine the applicability of the coupling interface to the prediction of the interaction of ship-induced waves with complex bathymetric and structural boundaries.

The remainder of this paper is structured as follows. In Section 2, the governing equations of the models REEF3D::SFLOW and REEF3D::CFD are presented and the approach of the newly developed coupling interface is introduced. For the sake of brevity, the term SFLOW is used when referring to REEF3D::SFLOW and CFD is used when referring to REEF3D::CFD in the remainder of the paper. In Section 3, verification test cases with a uniform bathymetry are presented, followed by a validation of the coupling in Section 5. In Section 5, an application of the SWE-CFD-HDC model to a complex ship wave structure interaction problem is presented. Finally, conclusions are drawn and an outlook is provided in Section 7.

2. Numerical methods

2.1. REEF3D::SFLOW

The shallow water equation solver SFLOW is designed for the efficient simulation of processes typically observed in many coastal, estuarine, or fluvial regions (Wang et al., 2020b). The solver is governed by a depth-averaged version of the continuity Eq. (1) and depth-averaged versions of the momentum-equations in all three coordinate directions (2)–(4).

$$\frac{\partial \zeta}{\partial t} + \frac{\partial h_S u}{\partial x} + \frac{\partial h_S v}{\partial y} = 0 \tag{1}$$

$$\frac{\partial u}{\partial t} + u\frac{\partial u}{\partial x} + v\frac{\partial u}{\partial y} = -g\frac{\partial \zeta}{\partial x} - \frac{1}{\rho h}\left(\frac{\partial hq}{\partial x} - \left(\frac{3}{2}q + \frac{1}{4}\rho h \phi_{nh}\right)\frac{\partial d}{\partial x}\right) \tag{2}$$

$$\frac{\partial v}{\partial t} + u\frac{\partial v}{\partial x} + v\frac{\partial v}{\partial y} = -g\frac{\partial \zeta}{\partial y} - \frac{1}{\rho h}\left(\frac{\partial hq}{\partial y} - \left(\frac{3}{2}q + \frac{1}{4}\rho h \phi_{nh}\right)\frac{\partial d}{\partial y}\right) \tag{3}$$

$$\frac{\partial w}{\partial t} + u\frac{\partial w}{\partial x} + v\frac{\partial w}{\partial y} = -\frac{1}{\rho h_S} - \left(\frac{3}{2}q + \frac{1}{4}\rho h_S \phi_{nh_S}\right) \tag{4}$$

In Eqs. (1)–(4), u, v, w are the depth-averaged velocity components in x-, y-, z-direction, respectively. p is the depth-averaged pressure, d is the water depth, ζ is the free surface elevation, and $h_S = d + \zeta$. Parameter t denotes the time, g the gravitational acceleration and ρ is the fluid density. The term $\frac{3}{2}q + \frac{1}{4}\rho h \phi_{nh}$ denotes the quadratic vertical pressure profile (Jeschke et al., 2017).

The SWE are limited in their application range through the depth-averaged assumption inherent to the underlying equations, i.e., a negligible vertical velocity component. This leads to three limitations in the application of SWE-models. Firstly, the lack of vertical velocity information can lead to an incorrect representation of a wave's dispersion characteristics, which is relevant for the representation of deep water wave characteristics (Brocchini, 2013). The absence of wave dispersion leads to waves that steepen, similar to waves affected by shallow water conditions. Secondly, steep bed level gradients can lead to strong vertical flow velocities, which cannot be represented in a SWE model. Hence, SWE models are limited in their application to relatively mildly changing bathymetries. The third limitation is the model's inability to describe a stratification of horizontal velocity components over the water depth, which might play an important role in many nearshore processes (e.g. Elsayed et al., 2022).

Due to the possibility to run SFLOW in a mode that is based on the non-hydrostatic version of the shallow-water equations, the aforementioned application limitations can partly be mitigated (Wang et al., 2020b,a). In the non-hydrostatic set of equations, the vertical velocity component is accounted for by a dynamic pressure term, which preserves information on the depth-averaged vertical velocity component. This renders SFLOW also applicable for the prediction of waves in intermediate-depth water conditions. Yet, the application of the non-hydrostatic equations is not always required. If the expected waves are of sufficient length, as e.g. long-period ship wakes, the application of the non-hydrostatic module does not lead to any accuracy gain (Dempwolff et al., 2022b).

2.2. REEF3D::CFD

The employed high-fidelity CFD model is a hydrodynamic solver based on the RANSE, describing the conservation of mass (see Eq. (5)) and momentum (see Eq. (6)).

$$\frac{\partial U_i}{\partial x_i} = 0, \tag{5}$$

$$\frac{\partial U_i}{\partial t} + U_j\frac{\partial U_i}{\partial x_j} = -\frac{1}{\rho}\frac{\partial P}{\partial x_i} + \frac{\partial}{\partial x_j}\left[(\nu + \nu_t)\left(\frac{\partial U_i}{\partial x_j} + \frac{\partial U_j}{\partial x_i}\right)\right] + g_i. \tag{6}$$

The CFD model uses a level set method to describe the free surface and the use of a ghost cell immersed boundary method to describe solid boundaries (Berthelsen and Faltinsen, 2008). High-order discretization schemes, such as the 5th-order WENO scheme for spatial discretization or the third-order Runge–Kutta scheme for temporal discretization, can be employed. Different turbulence models are available. In the present paper, a k-ω model is employed, making use of a turbulence damping scheme to avoid the production of excessive turbulence near the free surface (Naot and Rodi, 1982). In the employed CFD toolbox the use of the $k-\omega$ model is standard practice. For details on the implementation and validation, the interested reader is referred to Bihs et al. (2016), Wang et al. (2020a), Kamath et al. (2019).

2.3. Coupling interface

A commonly employed method to account for wave boundary conditions that is also frequently used in both solvers SFLOW and CFD is to impose the wave kinematics via relaxation zones (Jacobsen et al., 2012; Windt et al., 2019). With this approach, the flow velocities and the free surface elevation are directly prescribed within the relaxation zone (Bihs et al., 2016; Wang et al., 2020b). The values to be imposed are derived from the applicable wave theories of the respective input

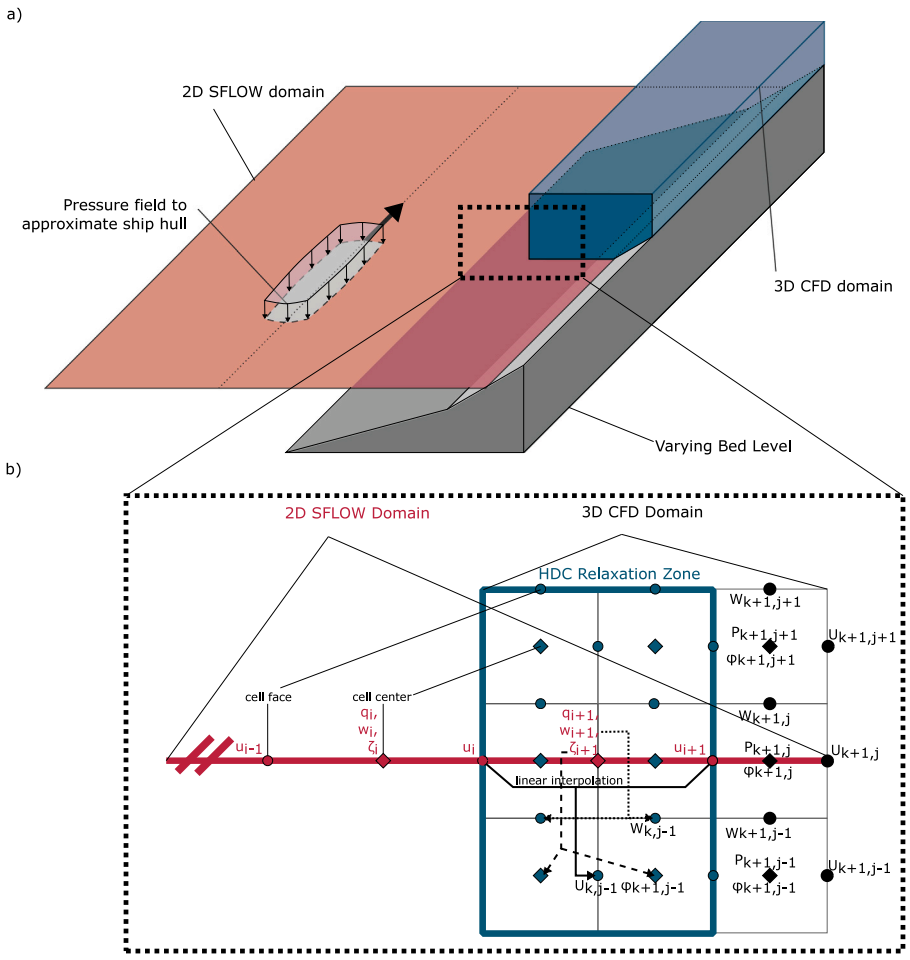

Fig. 1. (a) An illustration of the general concept of the coupling, highlighting the different models employed for primary wave prediction and indicating the dimensional mismatch between SFLOW and CFD; (b) a close-up view in the vertical cut plane of the interface between SFLOW and CFD indicating the information transfer on a grid level. The dots indicate the cell faces of the computational mesh and the rhombi the cell centers. Parameters u, w denote the depth-integrated velocities, ζ the free surface elevation, q the dynamic pressure, U, W the depth-resolved velocities, P is the depth-resolved pressure, and ϕ the signed distance variable of the level-set function used to describe the free surface. Parameters k, i and j denote the indices of the respective variables.

waves, governed by their length, height, and the water depth. Relaxation zones can also be included as numerical beaches to avoid wave reflection from the end of the numerical wave tank. In this case, the hydrodynamic quantities are prescribed by ramping the free surface and velocities down to still water conditions within the relaxation zone of typically two wavelengths (Miquel et al., 2018).

The newly developed coupling interface makes use of this relaxation zone method by deriving the CFD input from the results obtained with SFLOW; these results are then transferred to the CFD domain via a 3D relaxation zone consisting of a variable number of cells in all three spatial dimensions. The procedure is as follows: First, a simulation with SFLOW is run, and the corresponding hydrodynamic information is stored in a binary file ('state-file'). Then, these results of the free surface elevation and the velocity components, stored in the state-files are imposed in a relaxation zone of the CFD model. This means, that instead of imposing hydrodynamic information from specific theoretical wave theories, the information imposed in the CFD wave relaxation zone is derived from a numerical simulation with SFLOW. The coupling strategy, which is depicted in Fig. 1, can be described as a 2D-3D one-way coupling approach that restricts information transfer from the SWE domain into the inner CFD domain, per the implementation strategy. This procedure is particularly useful in cases where the input waves do not strictly follow any simple wave theory, such as waves that are strongly deformed due to the shallow water effects of shoaling, diffraction or refraction, or forced waves such as ship waves. As the intended application only focuses on the quantification of ship waves interacting with embankments and not on the examination of the interaction of reflected waves with the ship, a simpler one-way coupling is considered sufficient.

In Fig. 1 (b), the information transfer between SFLOW and CFD is depicted on a cell level. For the sake of simplicity, the drawing is reduced to a two-dimensional perspective, actually showing a 1D-2D coupling situation, excluding any cells in the x-y-plane. Therefore, the depicted information transfer does not account for the velocity-component v. Both models use staggered grids. In SFLOW, the depth-averaged horizontal velocities u (and v, but this direction is neglected due to the 2-dimensional nature of the drawing) are stored at the cell faces, while q, w, and ζ are stored in the cell centres. In the staggered grid of CFD, the velocities U, W (and V) are stored at the respective cell faces, while the signed distance function ϕ and the pressure P are stored at the cell centres. The information of the free surface η in SFLOW is transferred to the signed distance function ϕ for the level set function in the CFD model. Above the free water surface, i.e., in the air phase of the CFD model, no values are imposed such that the respective values develop only based on the equations in the water phase. Similarly, no values for the pressure P are imposed in the generation zone of the CFD model, but these values adapt automatically following the given velocity distribution. Due to the different mesh resolutions of the SFLOW model and CFD, interpolation of the data is required. Spatially, the input data is interpolated over the pre-defined

relaxation zone, as the CFD domain typically requires a higher mesh resolution than SFLOW. The temporal interpolation is adapted to the time-stepping of the CFD model. Together, the interpolated data is used as input conditions to the information in the relaxation zone of CFD.

The coupling used in this study works analogously to a HDC presented by Wang et al. (2022). Their work also uses a one-way hydrodynamic coupling interface for the fully nonlinear potential flow solver REEF3D::FNPF and REEF3D::CFD. The results of FNPF are stored in a binary state file and then imposed to the relaxation zone of the CFD domain. However, as both solvers calculate their result in three dimensions while employing differently resolved meshes, an additional vertical interpolation from the typically coarser mesh for the potential flow simulation to the higher resolved CFD simulation had to be included in the vertical coordinate direction.

In the hydrodynamic coupling interface between SFLOW and CFD introduced in the present study, the two models differ in the number of dimensions they describe. SFLOW uses depth-averaged velocities, while CFD simulates the 3D velocity field over time. This implies that the 3D solver requires information that is not present in the depth-averaged results. Mintgen and Manhart (2018) overcame this dimensional mismatch by applying a theoretical logarithmic velocity profile as input to the 3D domain. While this assumption holds for problems governed by uniform currents as often present in hydraulic engineering, the periodically oscillating velocity components underneath regular waves largely differ depending on the respective wave parameters. Therefore, the velocity profile in the relaxation zone of the coupled model cannot consistently be described by any one velocity distribution without knowing the underlying wave theory. Instead, for the coupling presented in this study, a constant vertical velocity distribution is assumed at first, which is hypothesized to align with physically more realistic velocity profiles at a sufficient distance to the relaxation zone. However, as no such coupling interface has yet been found for regular waves in the pertinent literature, further analysis of the evolution of the vertical profiles of the horizontal velocity within the numerical wave tank is required in order to examine if this hypothesis holds.

2.4. Assessment metrics

Various metrics are used within the present manuscript to examine the accuracy of the novel coupled approach and deviations to existing model approaches. In the following, the underlying equations are briefly introduced. The energy balance was examined in addition to the surface elevation and velocity distribution to ensure the energy transported is simulated correctly using Hughes' (2004) wave momentum flux parameter. This parameter quantifies the total energy imposed underneath a wave crest and is described in its non-dimensional form as follows:

$$M_{F,nd} = \left(\frac{\int_{-d}^{\eta(x)} (p_d + \rho U^2) dz}{\rho g d^2} \right)_{max}, \tag{7}$$

where parameter p_d denotes the dynamic pressure.

The mean absolute percentage error (MAPE) is used to quantify deviations between the SWE-CFD-HDC model and either the CFD model Section 3 or experimental data Section 5. In the present manuscript, it is calculated using the following equation:

$$\text{MAPE} = \frac{1}{n} \sum_{i=1}^{n} \left| \frac{y_{ref,i} - y_{calc,i}}{y_{ref,i}} \right|, \tag{8}$$

where parameter n refers to the number of data points, y_{ref} refers to the reference value (CFD or experimental), and y_{calc} to the value obtained with the SWE-CFD-HDC model.

Further, the root mean square error (RMSE) is used to provide an additional dimensional metric for deviations. Here, the deviations are considered with a power of 2, such that larger deviations get a higher weight than the smaller ones. The smaller the resulting value is, the closer the agreement between the calculated and the reference value. The underlying equation is the following:

$$\text{RMSE} = \sqrt{\frac{\sum_{i=1}^{n} (y_{ref,i} - y_{calc,i})^2}{n}} \tag{9}$$

Table 1
Model settings employed for the verification test cases.

–	CFD	SFLOW
CFL	0.2	0.2
dx	0.01 m	0.02 m
Turbulence model	$k-\omega$	none

3. Verification

Prior to the application of the developed HDC to complex engineering cases, verification and validation with simpler cases is required to ensure the model's performance when applied to benchmark cases. Therefore, a series of basic wave propagation test cases in a 2D wave flume setting was simulated, as suggested by Wang et al. (2020b). To assess the model performance, surface elevation and wave kinematics are examined. Two different regular waves with a wavelength of L = 4 m and a wave height of 0.01 m and 0.05 m in a water depth of 0.5 m described by different wave theories (linear, 2nd-order theory) and a solitary wave are simulated.

Firstly, a two-dimensional wave tank (x-z-plane), as depicted in Fig. 2, is set up using CFD to serve as a reference case for the accuracy of the SWE-CFD-HDC model. The length of the working zone (the area not occupied by relaxation zones) is set to 9 wavelengths (i.e., 36 m). A relaxation zone for wave generation l_{gen} of one wavelength is included between 0 m and 4 m and a relaxation zone for wave absorption of two wavelengths between 40 m and 48 m, as suggested by Miquel et al. (2018).

A second numerical wave tank is set up with SFLOW. This one is used to deliver the input data for the SWE-CFD-HDC model and further serves as reference data for the coupled simulations. Due to the model assumptions, this wave tank is only one-dimensional in x-direction. The dimensions equal the CFD wave tank with a relaxation zone of one wavelength (4 m) for wave generation, a working zone of 9 wavelengths (36 m), and a relaxation zone of two wavelengths (8 m) to serve as a numerical beach.

A third two-dimensional numerical wave tank in x-z-plane is set up with the CFD model, where the input is derived from the SFLOW model. This model setup will be referred to as SWE-CFD-HDC-model, describing a CFD model with input from SFLOW. This wave tank is shorter than the previously presented wave tanks starting at x = 12 m. A relaxation zone of l_{gen} = 4 m is included at the beginning of the wave tank between 12 m and 16 m to account for wave generation. In this relaxation zone, the hydrodynamic information for u, v, and η is imposed by the coupling interface, meaning that the information obtained from the previously described simulation with SFLOW is used as input information. At the end of the SWE-CFD-HDC-wave tank, a relaxation zone of two wavelengths is included.

In all these different numerical wave tanks, three velocity gauges are positioned. Gauge A is located in the middle of the HDC-relaxation zone for wave generation at x = 14 m, gauge B 2 m from the relaxation zone's end at x = 18 m, and gauge C at x = 26 m. The water-depth is set to 0.5 m. The total simulated time is 90 s, corresponding to 46 wave periods. Dedicated grid convergence studies, providing guidance for the required mesh resolution, were already performed by Moideen et al. (2019), Wang et al. (2020b,a). Consequently, corresponding values for the grid size dx and the CFL-criterion were used: 0.2 for the CFL criterion and a cell size of dx = 0.02 m for SFLOW and dx = 0.01 m for all CFD simulations. A standard $k-\omega$-turbulence model, as also applied by Bihs et al. (2016) and Wang et al. (2020a), is used in the CFD-simulations. A summary over the model settings is presented in Table 1

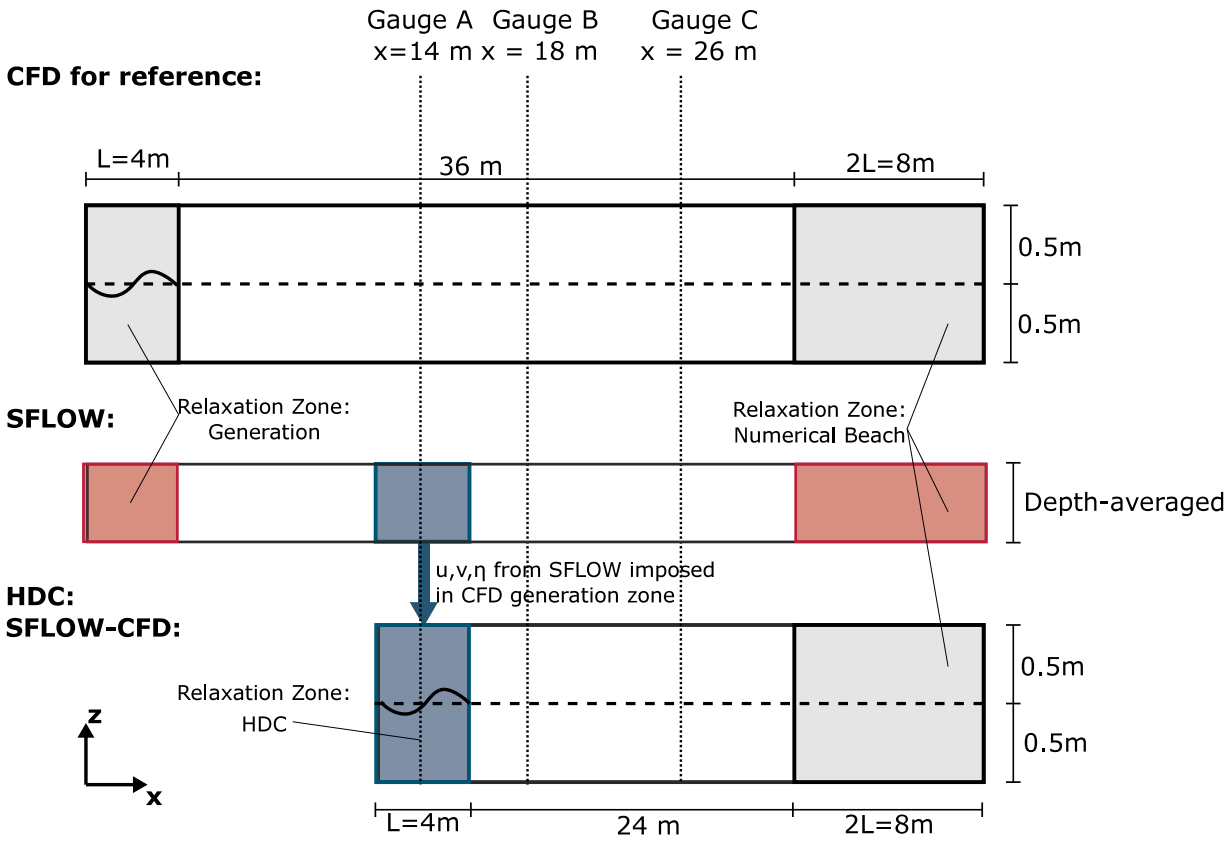

Fig. 2. Set up for the SWE-CFD-HDC numerical model test cases with a uniform bathymetry.

3.1. Linear waves

The first test case considers the propagation of a regular, linear wave with a wave height of 0.01 m and compares the individual results of the above described simulations runs, using CFD, SFLOW and the novel SWE-CFD-HDC model. Results are presented in Figs. 3 (a)–(d). Herein, Fig. 3 (a) displays the spatial free surface profile for the simulations using CFD and SFLOW, as well as the SWE-CFD-HDC model at time step $t = 87.5$ s. Additionally, the metrics of MAPE and RMSE are provided for the simulations with SFLOW and the SWE-CFD-HDC model. Here, the CFD model is used as reference for the quantification of the deviation. Fig. 3(b) - (d) show the vertical profiles of the horizontal velocity underneath the wave crests at the three gauges A–C for the CFD model and the SWE-CFD-HDC model. Additionally, the metric non-dimensionalized momentum flux parameter and the depth-averaged horizontal velocities are provided for the respective models.

The metrics indicate that the deviations of SFLOW and the SWE-CFD-HDC model compared to CFD are relatively low, with an MAPE below 5 % and an RMSE around 0.054 cm. The average deviations of the momentum flux parameter between the CFD-model and SWE-CFD-HDC-model equals 10.41 %. The vertical profiles of the horizontal velocity changes along the three gauges. While the velocity is more evenly distributed in the relaxation zone of the SWE-CFD-HDC model as shown at gauge A, it increasingly resembles the velocity distribution of the CFD model at gauges B and C.

3.2. Second order stokes waves

The second examined input wave is a regular wave with a height of 0.05 m, following Stokes 2nd-order theory (Dean and Dalrymple, 1991). Results are presented in Figs. 4 (a)–(d), following the same conventions as in Section 3.1. The MAPE shows a value of 3.99 % for the SWE-CFD-HDC model and an RMSE of 0.22 cm, in contrast to a MAPE of 2.92 % and an RMSE of 0.149 cm for the SFLOW simulation. The wave height of the three models, and the velocity profile of the CFD-model and the SWE-CFD-HDC model show only minor deviations, indicating a reliable performance of the novel SWE-CFD-HDC model. Again, the velocity profile of the SWE-CFD-HDC model aligns with the one from the CFD simulations with increasing distance from the wave generation relaxation zone.

3.3. Solitary wave

Finally, simulation results for a solitary wave with a height of 0.05 m are shown in Figs. 5 (a)–(e). A larger part of the wave tank is depicted, including an additional gauge (d), due to the solitary wave's length and propagation speed. The input waves are following third-order solitary wave theory, as presented by Fenton (1972). In Fig. 5 (a), the free surface profile is depicted at four different time steps, chosen such that the wave crest is located at the respective wave gauges. In Figs. 5 (b)–(e) the corresponding vertical profiles of the horizontal velocity are shown underneath the wave crest.

The error metrics examined for the four locations indicate a satisfying agreement between the three models, with deviations for the wave height between the SWE-CFD-HDC model and the CFD model below 2 %. As the velocity profile underneath a solitary wave is close to vertically evenly distributed, the differences between the SWE-CFD-HDC and the CFD velocity distribution are small throughout the whole domain, with deviations in the momentum flux parameter below 2 %. A summary of the resulting error metrics for the three verification test cases is given in Table 2

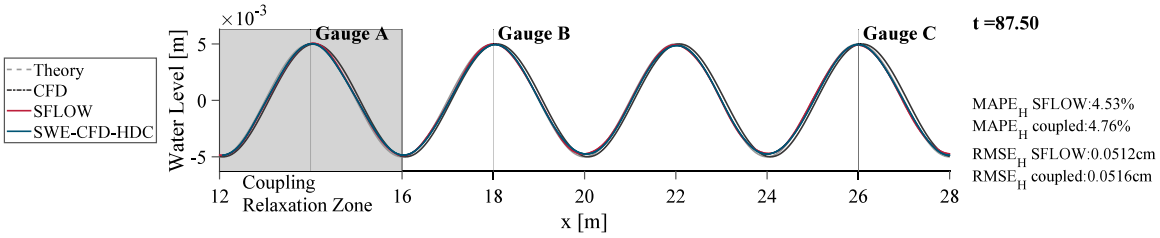

(a) Comparison of the instantaneous free water surface profile for a the different modules of the REEF3D toolbox.

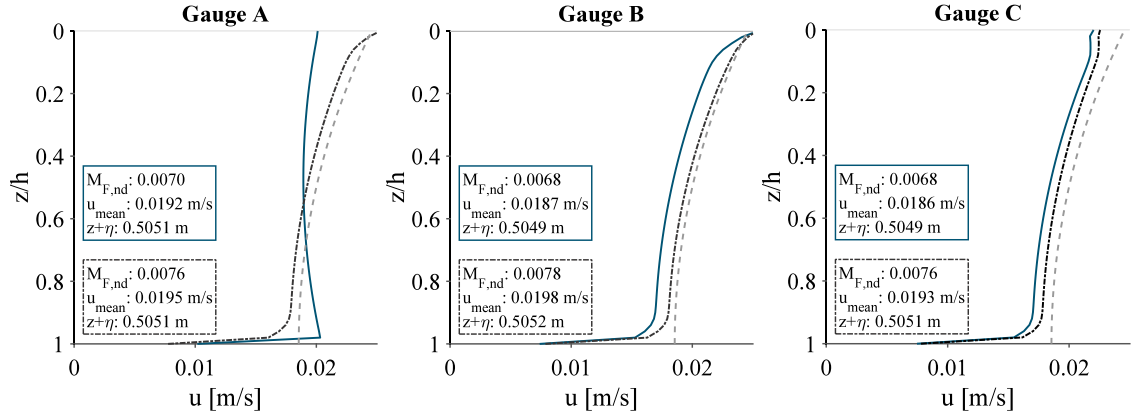

(b) Vertical profile of the horizontal velocity underneath a wave crest at Gauge A

(c) Vertical profile of the horizontal velocity underneath a wave crest at Gauge B

(d) Vertical profile of the horizontal velocity underneath a wave crest at Gauge C

Fig. 3. Results obtained with different REEF3D modules for the simulation of a linear wave propagating in a numerical wave tank at time step t = 87.5 s.

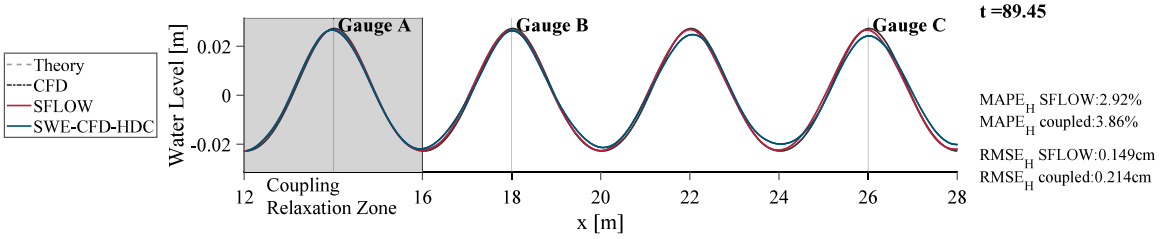

(a) Comparison of the instantaneous free water surface profile for a the different modules of the REEF3D toolbox.

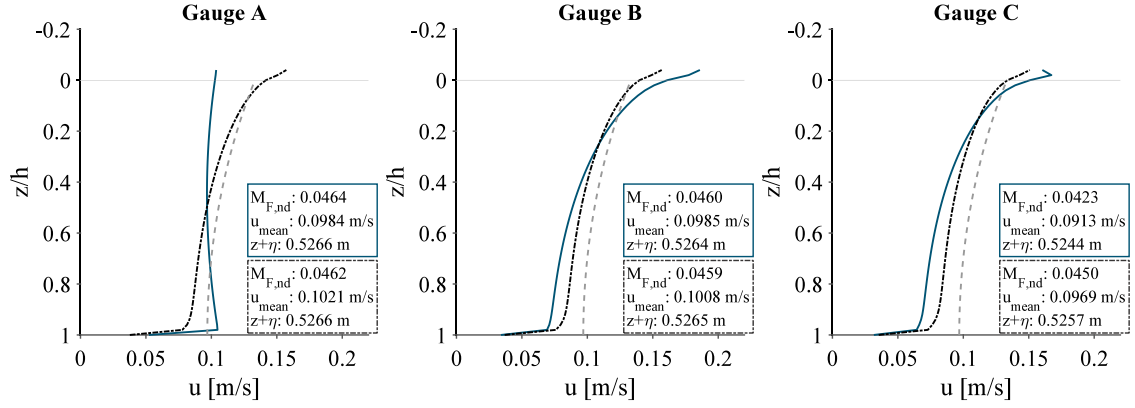

(b) Vertical profile of the horizontal velocity underneath a wave crest

(c) Vertical profile of the horizontal velocity underneath a wave crest

(d) Vertical profile of the horizontal velocity underneath a wave crest

Fig. 4. Results obtained with different REEF3D modules for the simulation of a 2nd-order Stokes wave propagating in a numerical wave tank at timestep t = 89.45 s .

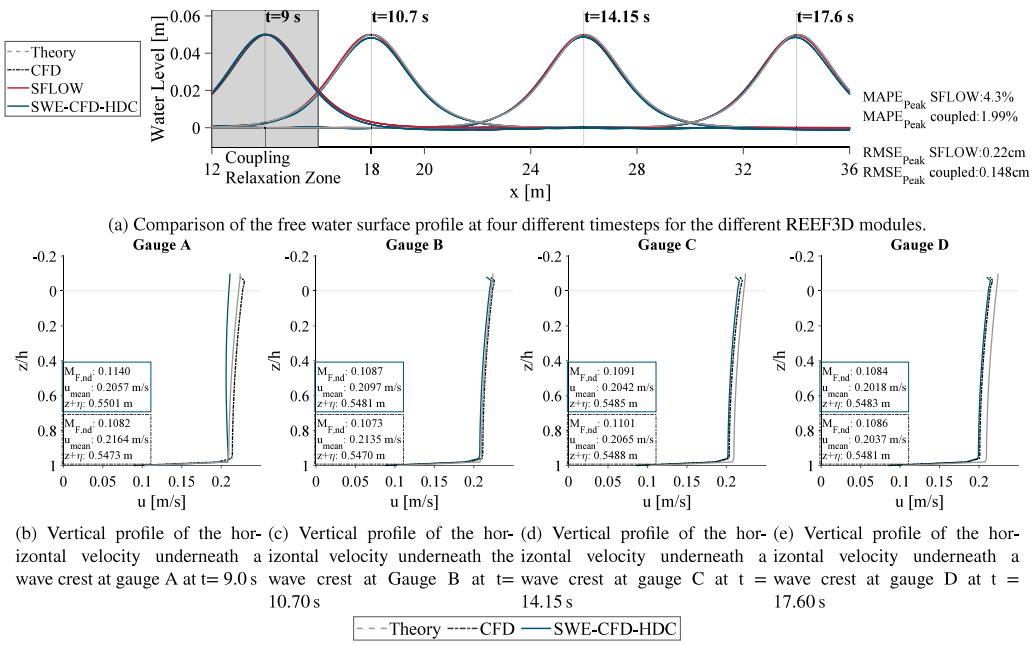

(a) Comparison of the free water surface profile at four different timesteps for the different REEF3D modules.

(b) Vertical profile of the horizontal velocity underneath a wave crest at gauge A at t= 9.0 s

(c) Vertical profile of the horizontal velocity underneath the wave crest at Gauge B at t= 10.70 s

(d) Vertical profile of the horizontal velocity underneath a wave crest at gauge C at t = 14.15 s

(e) Vertical profile of the horizontal velocity underneath a wave crest at gauge D at t = 17.60 s

Fig. 5. Results obtained with different REEF3D modules for the simulation of a solitary wave propagating in a numerical wave tank. The horizontal line refers to the still water level.

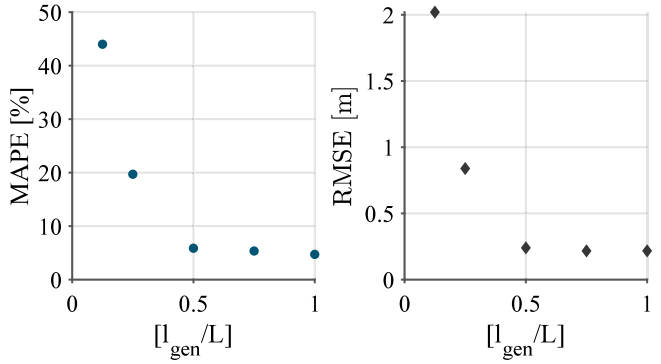

Fig. 6. Error metrics MAPE and RMSE for simulations of the 2nd-order Stokes wave with different lengths of the relaxation zone for wave generation of the SWE-CFD-HDC model.

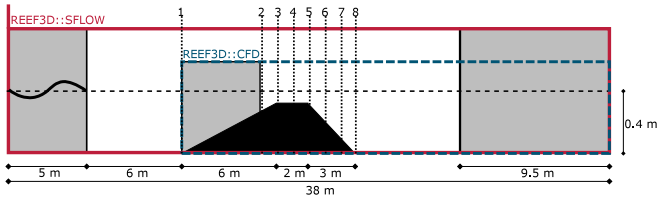

Fig. 7. Set up for the SWE-CFD-HDC numerical model to simulate wave propagation over a submerged bar.

3.4. Sensitivity study of the relaxation zone length

For typical theoretical input waves, the recommendation is to use relaxation zones for wave generation corresponding to one wavelength (Miquel et al., 2018). Similarly, a study by Wang et al. (2022) indicates a relaxation zone for coupled wave generation of one wavelength for a HDC between the potential flow solver FNPF and CFD. However, both of these input information for the relaxation zones rely on vertically resolved information for the velocity. Therefore, the coupling interface of a 2D-model to a 3D-model does not necessarily require the same relaxation zone dimensions. Consequently, a sensitivity study was carried out, examining the necessary relaxation zone length (l_{gen}) in the SWE-CFD-HDC model. A set of simulation runs was carried out with different lengths of the relaxation zone for the coupling. The 2nd order stokes wave with a height of 0.05 m and a length of 4 m, as in Section 3.2, serves as input for this study. The examined relaxation zone lengths were 0.5 m, 1.0 m, 2.0 m, 3.0 m and 4.0 m, corresponding to 0.125, 0.25, 0.5, 0.75 and 1.0 times the wavelength.

Table 2
Summary of the obtained error metrics of the SWE-CFD-HDC model compared to the CFD model.

Error metric	Linear	2nd-order stokes	Solitary
MAPE_{II} [%]	4.76	3.86	1.99
RMSE [cm]	0.0516	0.214	0.148
$\text{MAPE}_{M_{F,nd}}$ [%]	10.41	1.78	1.92

The resulting values for the MAPE and RMSE for the space averaged wave height at time step $t = 89.45$ for different lengths of the generation zone are shown in Fig. 6. It is evident that for $l_{\text{gen}} \geq 0.5 \cdot L$, both error metrics only change marginally for longer l_{gen}. For relaxation zones that are much shorter than $0.5 \cdot L$, the error rapidly increases, with wave heights largely underpredicted by the numerical model. This leads to the recommendation of employing a relaxation zone of at least half the wavelength in order to obtain accurate results with the SWE-CFD-HDC model.

4. Validation: wave propagation over a submerged bar

Herein, the simulation of waves propagating over a submerged bar serves as validation case. This is a commonly employed benchmark data set, based on the experimental work of Beji and Battjes (1993). During the validation of SFLOW (Wang et al., 2020a) it was found that SFLOW is able to simulate the wave deformation on the offshore side (decreasing water depth), but not behind the submerged bar (increasing water depth). This is in alignment with the inherent model assumptions. The subharmonic wave components are released after the wave propagation over the submerged bar. These wave components

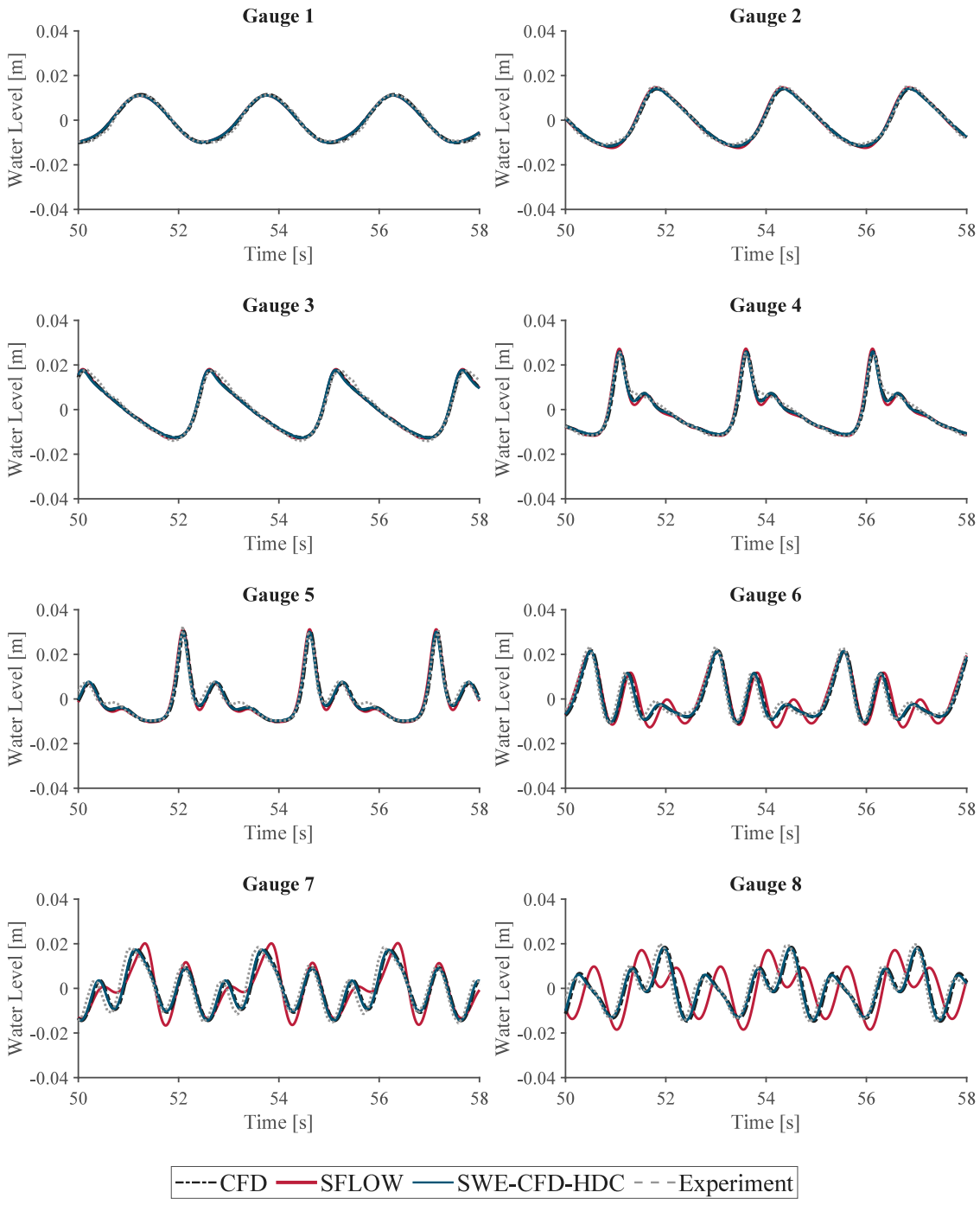

Fig. 8. Simulated and measured time-histories of the free surface elevation of a wave propagating over a submerged bar (Beji and Battjes, 1993).

have a relatively short wavelength and can, hence, not be described by shallow water theory and, thus, not be modelled by SFLOW. Therefore, this experimental benchmark data is suitable for the validation of the SWE-CFD-HDC model, as a significant accuracy gain is expected by employing the coupling over the SFLOW simulation, in particular behind the submerged bar.

The geometry and the gauge locations of the test case are shown in Fig. 7. The SFLOW wave tank consists of a 5 m wave relaxation zone and a 9.5 m dissipation zone. The submerged bar consists of a positive slope between 11 m and 17 m, a level crest between 17 m and 19 m, and a negative slope between 19 m and 22 m. A total of eight water level gauges are positioned along the submerged bar. The water depth is 0.4 m and the input wave a 2nd order Stokes wave with a height of $H = 0.021$ m and a period $T = 2.525$ s and a wave length of approximately $L = 4.8$ m, based on input parameters in Beji and Battjes (1993). The CFD wave tank of the SWE-CFD-HDC model starts at the beginning of the submerged bar. The relaxation zone is 5 m long and entirely positioned on the slope of the submerged bar, as indicated in Fig. 7. The CFD model used for reference employs the same set-up as the in the simulation with SFLOW.

The simulation with CFD takes 1.39 h, while the SWE-CFD-HDC, takes 1.13 h. This corresponds to a 19 % reduction of the computational time when employing the coupling in this specific case.

Results for the free surface time-histories of the three models compared to the experiments are presented in Fig. 8. All simulated and measured time-histories are in good agreement up to gauge 5, which

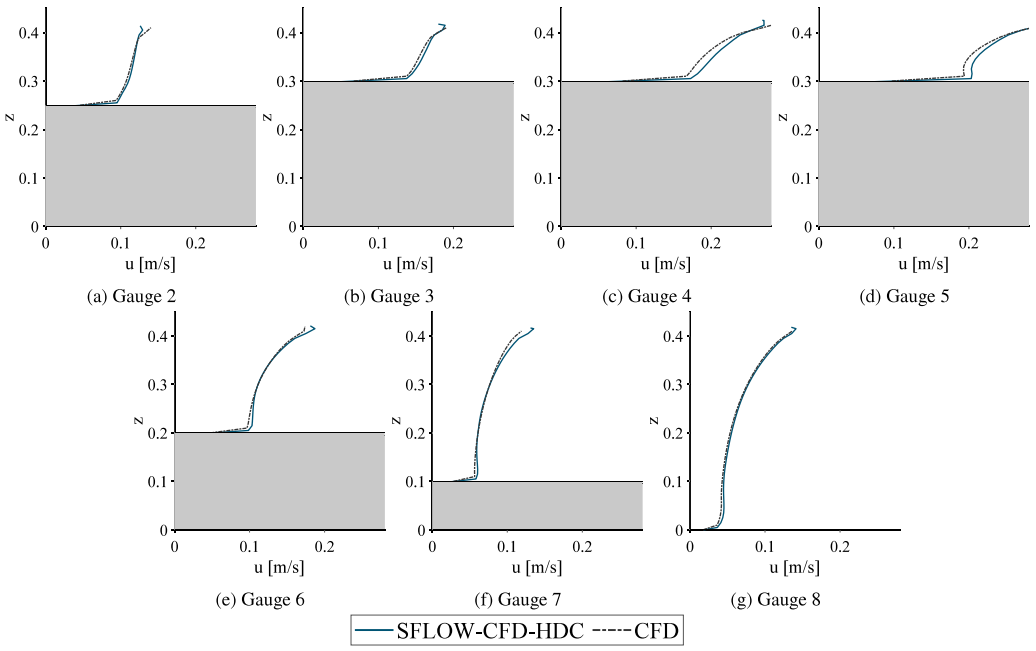

Fig. 9. Vertical profile of the horizontal velocities underneath the wave crest at the different gauge locations (Beji and Battjes, 1993).

is the last gauge positioned at the horizontal part of the submerged bar. At the remaining gauges (6, 7, 8), positioned in increasingly large water depth, the inaccuracy of SFLOW for simulating the high-frequency components becomes visible, as documented by Wang et al. (2020b). However, the SWE-CFD-HDC model shows almost perfect agreement with both the experimental data and CFD, indicating that the SWE-CFD-HDC model approach can overcome limitations of a SFLOW simulation.

In Figs. 9 (a)–(g), the vertical profiles of the horizontal velocity at the gauge locations are depicted. The experimental data set does not comprise velocity measurements, therefore only the SWE-CFD-HDC model and the CFD model are compared. No reliable information on the velocity profile at the beginning of the coupling zone could be extracted, thus gauge one is excluded from the analysis. Similar to the simple wave propagation test cases, the initial velocity profiles of the SWE-CFD-HDC model and CFD model differ slightly due to the initial velocity assumption in the SWE-CFD-HDC model. However, with increasing distance to the gauges, the deviations between the models reduce, so that for the gauges 4–8 almost no differences are visible anymore.

5. Application

5.1. Model set-up

To exploit the capabilities of the presented coupled modelling approach as a tool to predict ship-induced hydrodynamic loads, an application for determining the flow field around an estuarine groin is presented. This case study was chosen, as groins in parts of the Elbe estuary were found to be severely deteriorated by long-period ship waves. In particular, the primary wave height, defined as the water level gradient between the deepest point of the drawdown and the stern wave, was found to cause displacement of the rock armour due to overflow effects. For a detailed description of the damage observed and the driving mechanism of ship-induced overtopping see Melling et al. (2019) and Dempwolff et al. (2023). Before introducing the SWE-CFD-HDC, the boundary conditions for this overtopping event could only be approximated by using a very simplified load assumption (Dempwolff et al., 2023), neglecting important transient phenomena. Yet, the possibility of including a more realistic transient boundary condition of a ship-induced primary wave was not available. The SWE-CFD-HDC model now allows the use of a more realistic ship-generated flow field, simulated in SFLOW, to derive the necessary transient boundary conditions.

Table 3
Governing dimensions of the experimental model to study ship passage effects on estuarine groins.

–	Model	Prototype
Water depth	0.455 m	18.2 m
Ship draft	0.345 m	13.8 m
Ship breadth	1.375 m	55 m
Ship length	9.24 m	352 m
Ship speed	1.123 m	13.8 kn

To validate that the input time-histories of surface elevation from SFLOW represent physically sound conditions, an experimental data set from Bundesanstalt für Wasserbau (BAW)'s ship wave basin is used as a reference. This scaled model of a realistic navigation situation in the scale $1:40$ is shown in Fig. 10 (a) and a summary of the governing parameters is presented in Table 3. A model of a Post-PANAMAX container vessel (PPM55), at scale 1:40 as also used by Hun Ha and Gourlay (2018), Dempwolff et al. (2022c) navigates parallel along a mildly sloped (1:16) embankment. Along this embankment, several groins oriented perpendicular to the ship's direction of travel were constructed from grouted gravel. The ship speed was $1.123\,\mathrm{m\,s^{-1}}$, corresponding to $13.80\,\mathrm{kn}$ in prototype scale. Field observations revealed that most damage occurred when the water level exceeds the groin crest height (Melling et al., 2020), which is therefore considered in the set-up. The water level was measured with ultrasonic wave gauges at four locations around the groin. Additionally, the velocity components u and v were measured with electromagnetic current meters at two locations.

This setup was reproduced with the SWE-CFD-HDC model, as depicted in Fig. 10 (b). The entire ship wave basin was modelled with SFLOW using the free surface pressure term extension, to account for the processes of ship wave generation and propagation (Dempwolff et al., 2022c). The resulting transient and spatially-varying flow field for the velocity u and the water surface elevation η were then imposed to the relaxation zones of a $10\,\mathrm{m} \cdot 16\,\mathrm{m}$ CFD domain around the individual groin. The relaxation zones were considered at three

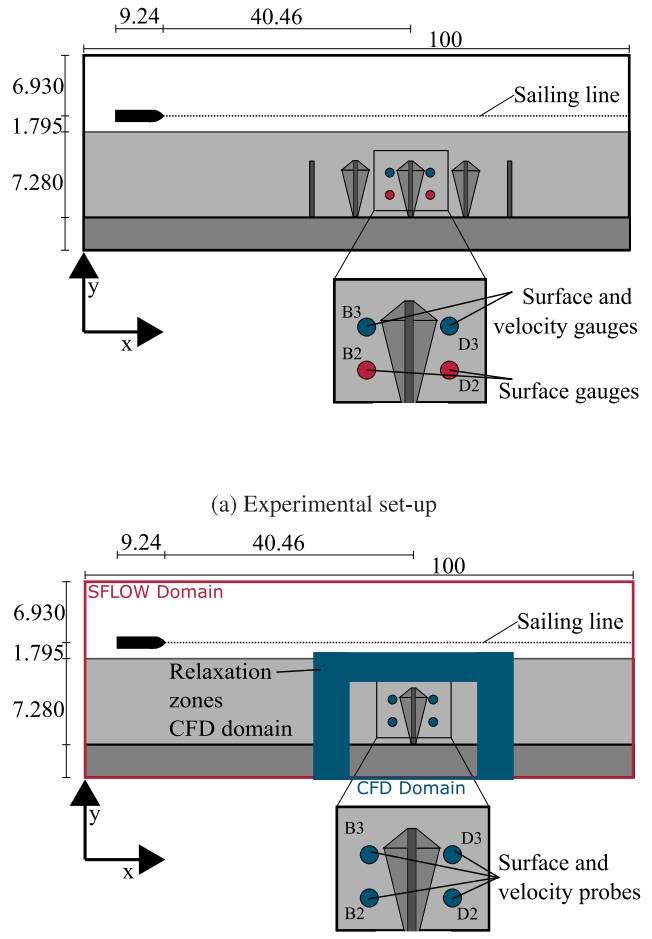

Fig. 10. Experimental and numerical model set-up used to study the interaction between ship-induced waves and groins. All dimensions in meters. (a) Experimental set-up where the straight sailing line is depicted, along with instrumentation. Blue circles indicate the position of combined surface-velocity gauges, and red circles indicate surface gauges in the facility. (b) Numerical set-up, showing the representation of the experimental conditions, and the domain boundaries for the individual model areas, with the red box showing the SFLOW domain, and the blue are depicting the relaxation zone that couples the SFLOW-to-CFD transition.

boundaries of the CFD domain, two of them perpendicular to the ship's motion trajectory and one parallel to it. As the length of the ship wave system corresponds to the length of the ship, a wavelength of 9.24 m is expected. Given the need to include half a wavelength as generation zone, as indicated by the sensitivity study presented in this paper, each relaxation zone has a length of 5 m. A locally refined mesh with a resolution of 1.5 cm in z-direction and 2.5 cm in x- and y-direction are employed around the groin is employed, resulting in 5.3 million computational cells. The coupled approach reduces the overall amount of computational cells by 86-percent as compared to an approach, where the whole ship wave basin would be represented with the CFD solver, thus significantly reducing the required computational run-time.

Despite the reduction in the number of computational cells, the area that had to be covered by the CFD domain had to be carefully chosen, given the current limitations of computational hardware. For the purpose of demonstrating the new coupling scheme, this study's focus is on the flow field around an individual groin structure that needs to be understood before further examination of interaction effects between multiple structures can take place. Aside from a focus on the single groin, the crest level had been lowered about 4 cm. For the use of the model results to derive design recommendations for estuarine groins, additional examinations regarding the numerical configuration, for example, detailed grid convergence, the placement and extent of the generation zones, and different surface roughness parameters, should be considered in a sensitivity study.

5.2. Modelling results

Qualitative results of the SWE-CFD-HDC model are presented in Fig. 11, highlighting the information exchange between SFLOW and CFD domain, at three different time steps. These correspond to the undisturbed flow field in Fig. 11 (a), the return current in Fig. 11 (b), and the overtopping due to the primary wave in Fig. 11 (c) (also see Dempwolff et al. (2023) for reference to the processes at these individual time steps). A detailed perspective view on the flow field during the overtopping process is presented in Figs. 12 (a) and (b). Fig. 12 (a) indicates the water surface elevation, showing the water level gradient present on both side of the groin at time step t = 446 s. Fig. 12 (b) indicates the surface velocities in x-direction and velocity vectors, respectively, at the same time step of most significant overtopping at time step t = 446 s. These results show qualitatively how large current velocities are induced over the whole length of the groin crest, even at modest water level gradients on each side of the groin, illustrating the damage potential of ship-induced waves acting on groins. These results and all following results are given in prototype scale to showcase the order of magnitude of the involved quantities in a real world setting.

Time-histories of the free surface elevation at four different gauges, two on either side of the individual groin, are presented in Fig. 13. In the experimental reference data, the shoaling process induced by the sloped embankment is clearly visible, leading to an increase in the primary wave amplitude in the vicinity of the embankment. In lee of the groin, the magnitude of the primary wave is reduced, owing to energy loss induced by the overtopping process. These phenomena are qualitatively reproduced with the CFD part of the SWE-CFD-HDC model, even though minor deviations in the exact quantities remain. Generally, the drawdown magnitude is slightly overestimated by the numerical model, while the stern wave height is underpredicted. The relevant qualitative processes are predicted reliably by the numerical model, with the phase of the wave signal closely agreeing with its experimental counterpart at all gauges. The differences in wave height between the gauges closer to the ship and the ones closer to the embankment, indicate that the spatially varying wave height due to shoaling is considered accurately in the coupled model approach. Behind the groin, the reduction of the primary wave height is qualitatively reproduced in the numerical model.

Time-histories for the velocity components u and v are presented in Fig. 14. Experimental reference data is only available for the gauges B3 and D3 (see Fig. 10). At these locations, the time-histories of the experiments and the numerical time-histories agree qualitatively. The time-histories of the velocity in y-direction reveal an asymmetry of the flow field, where the wave-facing side of the groin is characterized by an inflowing (negative) flow component after the maximum return current, while the gauges on the lee side of the groin show that an outflow from the groin field in positive coordinate direction takes place, reaching its peak at the maximum return current. At the gauges B2 and D2 (see Fig. 10), the gauges closer to the embankment, significant change of the velocities compared to the outer gauges can be observed. In particular, an increase of the maximum positive velocity in x-direction associated with the stern wave can be observed. This phenomenon cannot be validated, due to the lack of experimental velocity data, but since the water surface is predicted accurately at this location, it can be assumed that the hydrodynamic conditions at this location are reliably predicted. Furthermore, the increase of the maximum velocity closer to the embankment agrees qualitatively with the field observation that groin damage increases closer to the groin

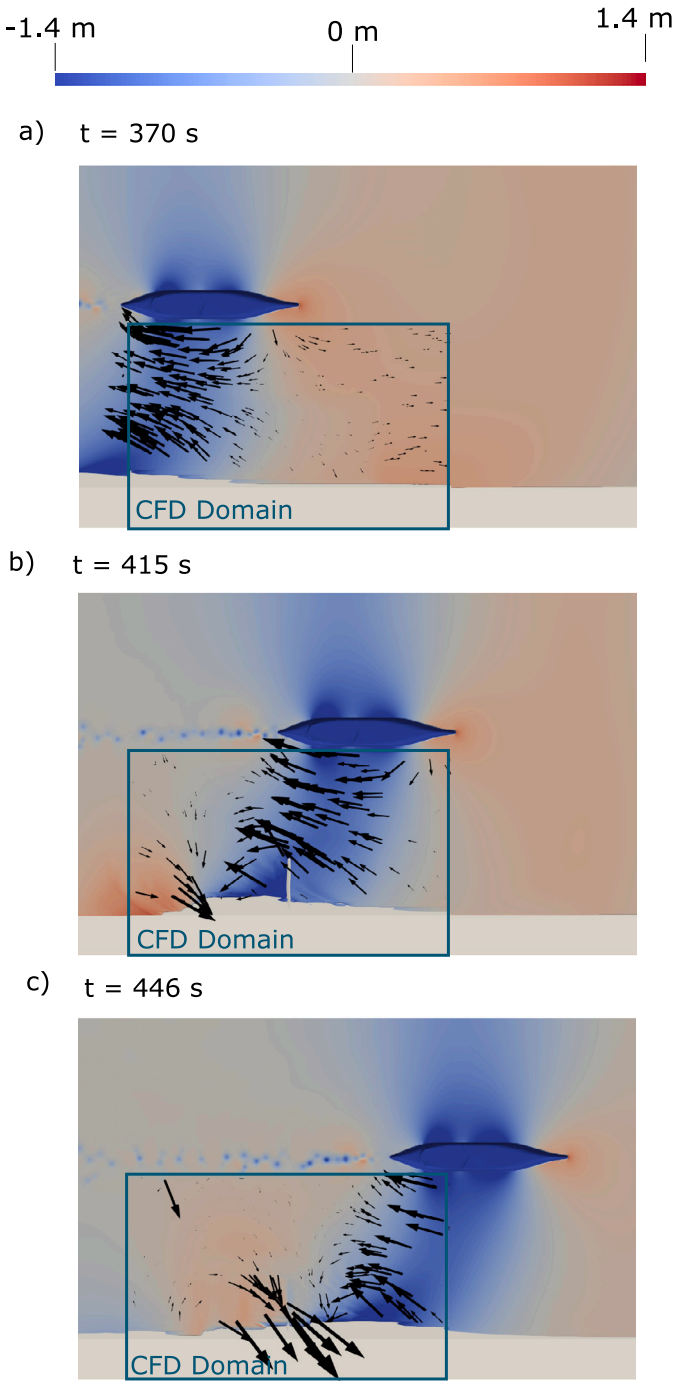

Fig. 11. SWE-CFD-HDC modelling results indicating the information exchange from the simulation including the ship hull in SFLOW to the smaller CFD domain along the embankment. The colour code depicts the surface elevation and the vectors of the surface current direction and magnitude.

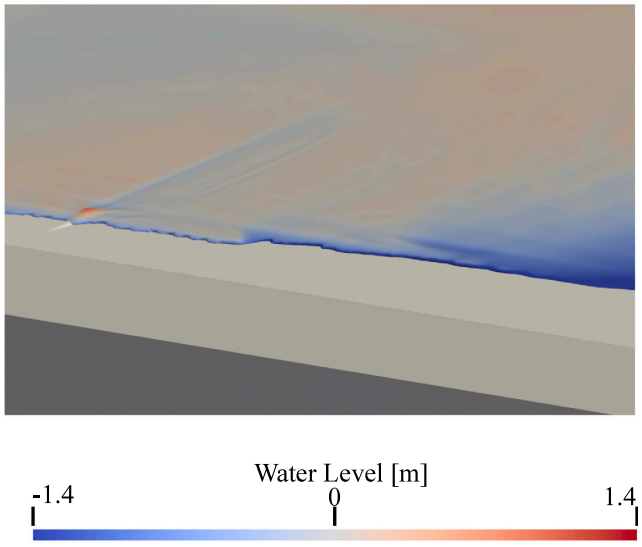

(a) Free surface elevation around an individual groin.

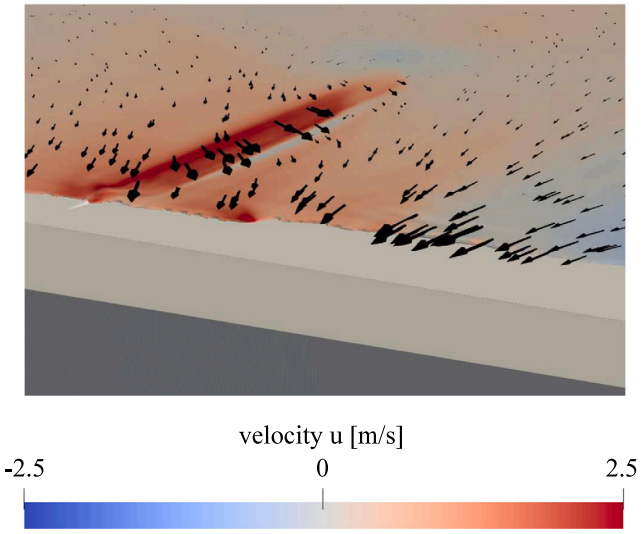

(b) Velocity field around an individual groin. The vectors indicate the orientation of the velocity field and the colour code indicates the velocity magnitude in x-direction.

Fig. 12. Perspective view on the groin at time step $t = 452$ s.

root (Melling et al., 2019). Behind the groin at gauge D2, the velocity-component u decreases drastically, which is in line with the observation that the groin overtopping process leads to a dampening of the primary wave system.

In Fig. 15 vertical profiles of the horizontal velocity u are presented for the return current (minimum negative velocity) and during the passage of the stern wave. These gauges are chosen since the local water surface prediction is in close agreement with the experimental data. The vertical profiles of the horizontal velocity in x and y-direction are close to a fairly evenly distributed, which is physically plausible due to the long period of the driving primary wave. However, in future work, it further needs to be examined if the vicinity of the relaxation zone affects this observation or if the velocity profile is already fully developed. Yet, a reference to an exact velocity profile is missing from the experimental data.

6. Discussion

The overarching goal of the presented coupling strategy is to reduce the overall computational effort while maintaining the accuracy of the results in locations where high-fidelity modelling is required to obtain good model-process-analogy. This reduction in computational effort can either be used to study the sensitivity of a certain construction to varying parameters or to allow obtaining a solution, if the case gets too large otherwise. The larger the domain is, the larger the potential to reduce the computational effort by employing simplified assumptions in certain regions. For the verification and validation cases presented in

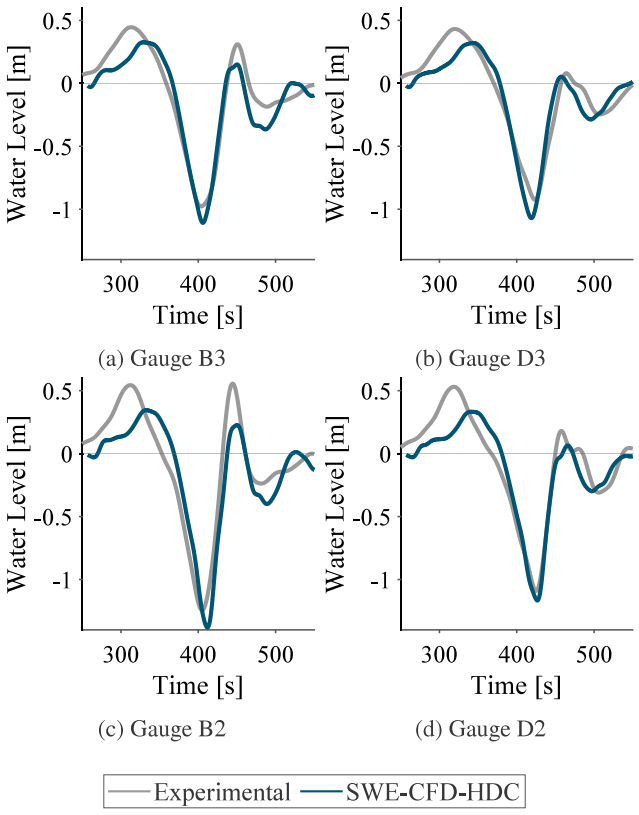

Fig. 13. Measured and simulated time-histories of the water surface elevation around a rock groin.

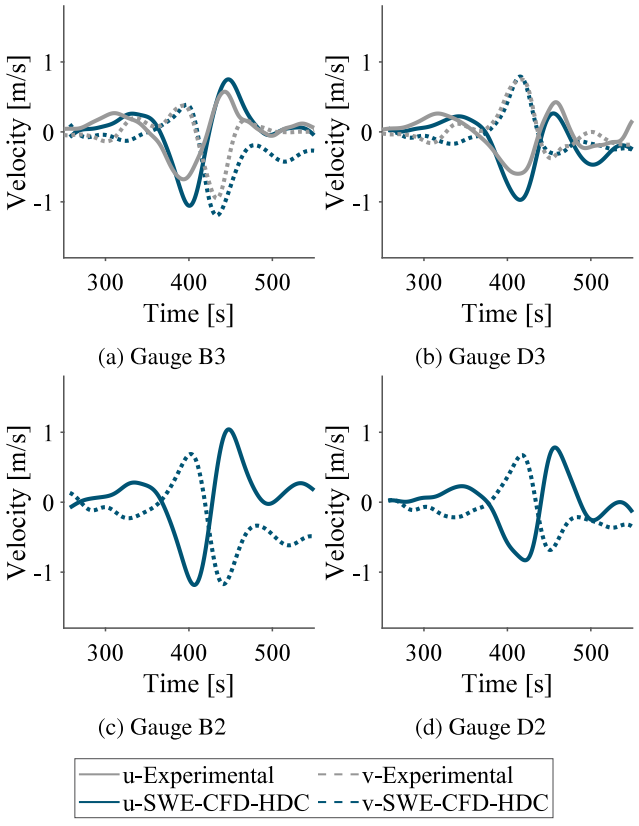

Fig. 14. Time-histories of the velocities around an individual groin during a ship passage.

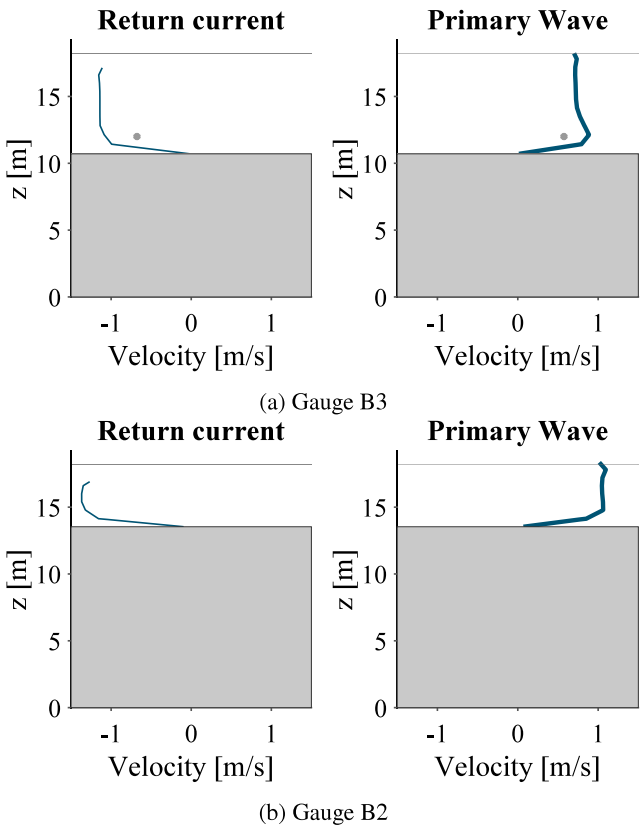

Fig. 15. Velocity profiles obtained from the SWE-CFD-HDC simulations.

this research, the reduction of computational effort is therefore rather limited, as these cases are based on comparatively small domains in the x-z-plane. In contrast, the application case of the ship wave simulation the computational domain required is large, truly showing the potential of the presented approach in reducing the computational effort. Given the present-day available computational hardware, a simulation of the whole wave basin at the presented grid resolution using CFD would barely be possible. Yet, the complex 3D geometry of the bathymetry, and the complexity of the incoming wave signal, exhibiting multidirectional features, as well as being transient and not following any simple wave theory does not allow any simplified loading assumption without significantly sacrificing parts of the underlying physics (Dempwolff et al., 2023).

This work's application case focuses on demonstrating the potential of the novel boundary conditions to overcome previous limitations. The prognosis of ship-induced groin overtopping is of high practical importance (Melling et al., 2019, 2020; Dempwolff et al., 2022a, 2023), such that exploitation of the presented showcase can form the basis for future improvements of groin design. The exact simulation of the overtopping layer may require an even higher mesh resolution, as this layer is very thin. This probably explains the remaining inaccuracies in the exact prediction of the drawdown and stern wave height. However, these resolution issues are not related to the coupling approach per se but rather stem from an unfavourable relation of still water level to groin crest height, in this very specific case of groin overtopping. The simulation of wind wave overtopping in RANSE-CFD-simulations typically require extremely high mesh resolution near the crest, therefore simulations are mostly performed in 2DV-mode neglecting components in y-direction (e.g. Chen et al., 2022; Mata and Van Gent, 2023). Due to the 3D nature of ship wave propagation, a corresponding dimensional reduction for primary wave simulation would not be possible, without further work on the quantification of the error induced.

Due to the large domain size of the 3D-CFD simulation, the computational effort of the coupled simulation is largely governed by this CFD-simulation. Neglecting the different numbers of cores occupied by the respective simulation, the CFD-share occupies 91.6 % of the simulation time. Considering the number of computational cores employed, this corresponds to 97.0 % of the overall computational effort. These numbers indicate, that for future model developments, the largest potential for reducing computational run-times resides within the CFD-part of the SWE-CFD-HDC approach. Further development of the solver, but also optimal model set-up, therefore needs to focus on the efficient use of the CFD-domain, reducing the cell count as much as feasible by choosing appropriate domain dimensions and further investigating optimal grid configurations.

In the current version of the SWE-CFD-HDC the information transfer is based on relaxation zones. While this approach is known for its reduction of reflection (Miquel et al., 2018), it requires additional space in the computational domain, increasing the number of computational cells, in particular when long waves such as ship waves are simulated. To a certain degree, this contradicts the idea of the presented coupling scheme, in reducing the computational effort. The experience from further application of the SWE-CFD-HDC model will show if this issue shows to be prohibitive in model application and if further implementation of Dirichlet-type coupling interfaces will be required.

When discussing the limitations imposed by the one-way coupling, the desired application needs to be considered. Generally, one-way coupling has shown sufficient for a range of applications where the additional fidelity from RANSE models is only required within a small subdomain Paulsen et al. (2014), Chen et al. (2022), Mata and Van Gent (2023). A direct comparison between a one-way and a two-way interface of the 2D-3D-RANSE-coupling of Di Paolo et al. (2021a) shows that some minor differences arise between these interfaces. However, these deviations are generally small, one-way and two-way coupling resulting in deviations between 3 % compared to a full 3D simulation. For the presented application case of far-field ship wave prediction no limitations arising from the one-way coupling could be identified. In the suggested model set-up the SFLOW domain covers the whole area between the ship and the embankment, which means that wave reflection is accounted for in the SWE-solver. Additional reflections only included in the CFD domain are sought to be negligible in this specific case. In addition, the pressure term is a simplified manner to account for ship wave generation, such that the effect of incoming waves such as reflected waves acting on a ship cannot be quantified. As the ship hydrodynamics in confined waterways is not the focus of this work, but rather the ship-induced loads acting on the embankments, these limitations do not conflict with the purpose of the suggested method.

7. Conclusions and outlook

In this study, a novel hydrodynamic coupling interface between the shallow-water-equation solver REEF3D::SFLOW and the 3D-RANS-equation solver REEF3D::CFD is presented. The coupling interface is based on a one-way coupling approach, where the results from the SWE-solver are imposed in a relaxation zone of the CFD simulation. The coupling interface is proposed for wave propagation problems, where processes take place on multiple scales. Typically, this would be the case for waves approaching some complex shoreline, where shallow water deformation processes (shoaling, refraction, diffraction) change the incoming wave properties before these waves further interact with complex 3-dimensional structures near the embankments. Long-period ship-induced waves, which deform during their propagation in the surrounding waterway, are a specific example of such a multi-scale problem, and improving the prediction of such waves and their effects on embankments was the main driver for implementing the coupling interface.

With respect to the objectives pursued in this study, the following conclusions can be drawn:

- **Verification and validation:** Some verification test cases for regular waves following linear wave theory and 2nd-order stokes wave theory, as well as solitary wave theory, are presented. The model performance of these cases indicates that imposing the results for the free surface elevation and the velocities from SFLOW works as a reliable boundary condition for the CFD domain, as resulting deviations from a theoretical input wave to a CFD simulation considering the energy balance, and wave heights are small. The validation test case of wave propagation over a submerged bar shows that the SWE-CFD-HDC simulation approach can overcome the limitations of a shallow water equation solver when it comes to the prediction of the subharmonic wave components behind the submerged bar. Furthermore, this validation case shows that imposing hydrodynamic information in the relaxation zone even works when the bathymetry leads to varying water depths within the generation zone.
- **2D-3D-mismatch:** As the velocity components contained in the SWE-solution are depth-averaged, no information on the vertical profile is contained. In contrast, the RANSE solver includes this information as it solves the equations in all coordinate directions. Therefore, this mismatch of the dimensions considered in the solvers had to be examined. With increasing distance to the relaxation zone, the initially assumed constant vertical velocity profiles align with the theoretical ones and the ones from a CFD simulation. A sensitivity study further indicates that the relaxation zone length, where the results from SFLOW are imposed, should at least be at a minimum a half of the input wavelength.
- **Applicability to ship-induced waves:** The application of the suggested model to a case of groin overtopping due to a complex ship-induced wave input signal indicates the applicability of the novel approach to derive design-relevant information for estuarine infrastructure due to ship-induced waves. The overtopping is qualitatively in agreement with processes observed in the field, and a comparison of measurements obtained from an experiment for the free surface and the velocity further stresses the model's prognostic accuracy. Compared to a SWE solution obtained with SFLOW, a large advantage is that velocity profiles can be obtained. The velocity distribution underneath a wave is very important to quantify the shear stress and, hence, the erosion potential of a wave-induced flow field. When using a depth-averaged model such as SFLOW it would not be possible to directly obtain this crucial information. Therefore, 3-dimensional models such as REEF3D::CFD need to be employed to study the velocity profiles associated with ship-induced waves. After further validation, this information can contribute to further understand and quantify the waves' damage potential. The coupled REEF3D framework, hence, presents itself as an attractive tool that can complement existing methods for the prediction of ship-induced loads.
- **Future Work:**
  The presented results indicate the new potential of this method for the prediction of ship-induced loads. To ensure that loads are predicted within a wide range of parameter values, and the sensitivity to varying boundary conditions is accurately reflected within the numerical model, further tests and validation studies are required. In particular, the vertical velocity distribution underneath a ship-induced primary wave should be studied in detail to be able to derive sound conclusions on the erosion potential of ship waves close to embankments. A second potential line of research is the analysis of different mitigation strategies to reduce the damage to engineering structures due to ship-induced primary waves. These mitigation strategies may cover the inclusion of nature-based solutions near waterway embankments, as well as variations of ship speed to name some commonly mentioned ideas. After further successful validation, the presented tool may be applied to these varying questions of waterway design and therefore help to balance the economic needs of ship traffic with robust and environmentally valuable waterways.

Funding

This study is part of the research project NumSiSSI (Numerical Simulation of Shipwave–Structure-Interaction in Coastal Areas) conducted in cooperation with the German Federal Waterways Engineering and Research Institute (BAW)

CRediT authorship contribution statement

León-Carlos Dempwolff: Conceptualization, Formal analysis, Methodology, Validation, Visualization, Writing – original draft. **Christian Windt:** Conceptualization, Methodology, Validation, Writing – review & editing. **Hans Bihs:** Conceptualization, Software, Validation, Writing – review & editing. **Gregor Melling:** Conceptualization, Investigation, Writing – review & editing. **Ingrid Holzwarth:** Conceptualization, Funding acquisition, Methodology, Project administration, Supervision, Writing – review & editing. **Nils Goseberg:** Conceptualization, Funding acquisition, Methodology, Project administration, Resources, Supervision, Writing – review & editing.

Declaration of competing interest

The authors declare that they have no known competing financial interests or personal relationships that could have appeared to influence the work reported in this paper.

Data availability

Data will be made available on request.

References

Aggarwal, A., Tomaselli, P.D., Christensen, E.D., Bihs, H., 2020. Computational fluid dynamics investigations of breaking focused wave-induced loads on a monopile and the effect of breaker location. J. Offshore Mech. Arct. Eng. 142 (2), 021903. http://dx.doi.org/10.1115/1.4045187.

Almström, B., Larson, M., 2020. Measurements and analysis of primary ship waves in the stockholm archipelago, Sweden. J. Mar. Sci. Eng. 8 (10), 743. http://dx.doi.org/10.3390/jmse8100743.

Almström, B., Roelvink, D., Larson, M., 2021. Predicting ship waves in sheltered waterways – an application of XBeach to the Stockholm Archipelago, Sweden. Coast. Eng. 170, 104026. http://dx.doi.org/10.1016/j.coastaleng.2021.104026.

Bayraktar Ersan, D., Beji, S., 2013. Numerical simulation of waves generated by a moving pressure field. Ocean Eng. 59, 231–239. http://dx.doi.org/10.1016/j.oceaneng.2012.12.025.

Beji, S., Battjes, J., 1993. Experimental investigation of wave propagation over a bar. Coast. Eng. 19 (1–2), 151–162. http://dx.doi.org/10.1016/0378-3839(93)90022-Z.

Bellafiore, D., Zaggia, L., Broglia, R., Ferrarin, C., Barbariol, F., Zaghi, S., Lorenzetti, G., Manfè, G., De Pascalis, F., Benetazzo, A., 2018. Modeling ship-induced waves in shallow water systems: The Venice experiment. Ocean Eng. 155, 227–239. http://dx.doi.org/10.1016/j.oceaneng.2018.02.039.

Berthelsen, P.A., Faltinsen, O.M., 2008. A local directional ghost cell approach for incompressible viscous flow problems with irregular boundaries. J. Comput. Phys. 227 (9), 4354–4397. http://dx.doi.org/10.1016/j.jcp.2007.12.022.

Biausser, B., Fraunié, P., Grilli, S., Marcer, R., 2004. Numerical analysis of the internal kinematics and dynamics of three-dimensional breaking waves on slopes. Int. J. Offshore Polar Engng. 14, 247–256.

Bihs, H., Kamath, A., Alagan Chella, M., Aggarwal, A., Arntsen, Ø.A., 2016. A new level set numerical wave tank with improved density interpolation for complex wave hydrodynamics. Comput. & Fluids 140, 191–208. http://dx.doi.org/10.1016/j.compfluid.2016.09.012.

Brocchini, M., 2013. A reasoned overview on Boussinesq-type models: The interplay between physics, mathematics and numerics. Proc. R. Soc. A: Math., Phys. Eng. Sci. 469 (2160), 20130496. http://dx.doi.org/10.1098/rspa.2013.0496.

Chella, M.A., Bihs, H., Myrhaug, D., Arntsen, Ø.A., 2019. Numerical modeling of breaking wave kinematics and wave impact pressures on a vertical slender cylinder. J. Offshore Mech. Arct. Eng. 141 (5), 051802. http://dx.doi.org/10.1115/1.4042265.

Chen, Y.-Y., Li, M.-S., 2015. Evolution of breaking waves on sloping beaches. Coast. Eng. 95, 51–65. http://dx.doi.org/10.1016/j.coastaleng.2014.09.002.

Chen, W., Warmink, J., Van Gent, M., Hulscher, S., 2022. Numerical investigation of the effects of roughness, a berm and oblique waves on wave overtopping processes at dikes. Appl. Ocean Res. 118, 102971. http://dx.doi.org/10.1016/j.apor.2021.102971.

Choi, Y., 2019. Two-way coupling between potential and viscous flows for a marine application. https://www.researchgate.net/publication/338913718_Two-way_Coupling_between_Potential_and_Viscous_Flows_for_a_Marine_Application.

David, C.G., Roeber, V., Goseberg, N., Schlurmann, T., 2017. Generation and propagation of ship-Borne waves - solutions from a Boussinesq-type model. Coast. Eng. 127, 170–187. http://dx.doi.org/10.1016/j.coastaleng.2017.07.001.

David, C.G., Schlurmann, T., 2020. Hydrodynamic drivers and morphological responses on small coral islands—the thoondu spit on Fuvahmulah, the Maldives. Front. Mar. Sci. 7, 538675. http://dx.doi.org/10.3389/fmars.2020.538675.

Dean, R.G., Dalrymple, R.A., 1991. Water Wave Mechanics for Engineers and Scientists. In: Advanced Series on Ocean Engineering, vol. 2, World Scientific, http://dx.doi.org/10.1142/1232.

Dempwolff, L.-C., Melling, G., Windt, C., Lojek, O., Martin, T., Holzwarth, I., Bihs, H., Goseberg, N., 2022a. Loads and effects of ship-generated, drawdown waves in confined waterways - A review of current knowledge and methods. J. Coast. Hydraul. Struct. 2, 46. http://dx.doi.org/10.48438/jchs.2022.0013.

Dempwolff, L.-C., Windt, C., Goseberg, N., Martin, T., Bihs, H., Melling, G., 2022b. Verification of a free-surface pressure term extension to represent ships in a non-hydrostatic shallow-water-equations solver. J. Offshore Mech. Arct. Eng. 1–12. http://dx.doi.org/10.1115/1.4056121.

Dempwolff, L.-C., Windt, C., Melling, G., Bihs, H., Holzwarth, I., Goseberg, N., 2023. Ship wave–induced hydraulic loading on estuarine groins: A conceptual numerical study. J. Waterw. Port Coast. Ocean Eng. 149 (3), 04023002. http://dx.doi.org/10.1061/JWPED5.WWENG-1937.

Dempwolff, L.-C., Windt, C., Melling, G., Martin, T., Bihs, H., Holzwarth, I., Goseberg, N., 2022c. The influence of the hull representation for modelling of primary ship waves with a shallow-water equation solver. Ocean Eng. 266, 113163. http://dx.doi.org/10.1016/j.oceaneng.2022.113163.

Di Paolo, B., Lara, J.L., Barajas, G., Losada, Í.J., 2021a. Wave and structure interaction using multi-domain couplings for Navier-Stokes solvers in OpenFOAM®. Part I: implementation and validation. Coast. Eng. 164, 103799. http://dx.doi.org/10.1016/j.coastaleng.2020.103799.

Di Paolo, B., Lara, J.L., Barajas, G., Losada, Í.J., 2021b. Waves and structure interaction using multi-domain couplings for Navier-Stokes solvers in OpenFOAM®. Part II: validation and application to complex cases. Coast. Eng. 164, 103818. http://dx.doi.org/10.1016/j.coastaleng.2020.103818.

Du, P., Ouahsine, A., Sergent, P., Hu, H., 2020. Resistance and wave characterizations of inland vessels in the fully-confined waterway. Ocean Eng. 210, 107580. http://dx.doi.org/10.1016/j.oceaneng.2020.107580.

Elfrink, B., Baldock, T., 2002. Hydrodynamics and sediment transport in the swash zone: A review and perspectives. Coast. Eng. 45 (3–4), 149–167. http://dx.doi.org/10.1016/S0378-3839(02)00032-7.

Elsayed, S.M., Gijsman, R., Schlurmann, T., Goseberg, N., 2022. Nonhydrostatic numerical modeling of fixed and mobile barred beaches: limitations of depth-averaged wave resolving models around sandbars. J. Waterw. Port Coast. Ocean Eng. 148 (1), 04021045. http://dx.doi.org/10.1061/(ASCE)WW.1943-5460.0000685.

Fenton, J., 1972. A ninth-order solution for the solitary wave. J. Fluid Mech. 53 (2), 257–271. http://dx.doi.org/10.1017/S002211207200014X.

Fleit, G., Baranya, S., Krámer, T., Bihs, H., Józsa, J., 2019. A practical framework to assess the hydrodynamic impact of ship waves on river banks. River Res. Appl. 35 (9), 1428–1442. http://dx.doi.org/10.1002/rra.3522.

Fleit, G., Baranya, S., Rüther, N., Bihs, H., Krámer, T., Józsa, J., 2016. Investigation of the effects of ship induced waves on the littoral zone with field measurements and CFD modeling. Water 8 (7), 300. http://dx.doi.org/10.3390/w8070300.

Forlini, C., Qayyum, R., Malej, M., Lam, M.-A.Y.-H., Shi, F., Angelini, C., Sheremet, A., 2021. On the problem of modeling the boat wake climate: the florida intracoastal waterway. J. Geophys. Res.: Oceans 126 (2), http://dx.doi.org/10.1029/2020JC016676.

Gao, Y., Zhu, J., Wang, L., Li, W., 2023. Experimental investigation of breaking regular waves slamming on offshore wind jacket structure. Ocean Eng. 279, 114528. http://dx.doi.org/10.1016/j.oceaneng.2023.114528.

Govindasamy, V.K., Chella, M.A., Sannasi Annamalaisamy, S., Rajamanickam, P.S., 2023. Impact pressure distribution and characteristics of breaking wave impact on a monopile. Ocean Eng. 271, 113771. http://dx.doi.org/10.1016/j.oceaneng.2023.113771.

Hattori, M., Arami, A., Yui, T., 1994. Wave impact pressure on vertical walls under breaking waves of various types. Coast. Eng. 22 (1–2), 79–114. http://dx.doi.org/10.1016/0378-3839(94)90049-3.

Hughes, S.A., 2004. Wave momentum flux parameter: A descriptor for nearshore waves. Coast. Eng. 51 (11–12), 1067–1084. http://dx.doi.org/10.1016/j.coastaleng.2004.07.025.

Hun Ha, J., Gourlay, T., 2018. Validation of container ship squat modeling using full-scale trials at the port of fremantle. J. Waterw. Port Coast. Ocean Eng. 144 (1), 04017037. http://dx.doi.org/10.1061/(ASCE)WW.1943-5460.0000425.

Jacobsen, N.G., Fuhrman, D.R., Fredsøe, J., 2012. A wave generation toolbox for the open-source CFD library: OpenFoam®: Wave generation toolbox. Internat. J. Numer. Methods Fluids 70 (9), 1073–1088. http://dx.doi.org/10.1002/fld.2726.

Jeschke, A., Pedersen, G.K., Vater, S., Behrens, J., 2017. Depth-averaged non-hydrostatic extension for shallow water equations with quadratic vertical pressure profile: Equivalence to Boussinesq-type equations. Internat. J. Numer. Methods Fluids 84 (10), 569–583. http://dx.doi.org/10.1002/fld.4361.

Kamath, A., Fleit, G., Bihs, H., 2019. Investigation of free surface turbulence damping in RANS simulations for complex free surface flows. Water 11 (3), 456. http://dx.doi.org/10.3390/w11030456.

Kamath, A., Roy, T., Seiffert, B.R., Bihs, H., 2022. Experimental and numerical study of waves breaking over a submerged three-dimensional bar. J. Waterw. Port Coast. Ocean Eng. 148 (2), 04021052. http://dx.doi.org/10.1061/(ASCE)WW.1943-5460.0000697.

Keimer, K., Schürenkamp, D., Miescke, F., Kosmalla, V., Lojek, O., Goseberg, N., 2021. Ecohydraulics of surrogate salt marshes for coastal protection: wave–vegetation interaction and related hydrodynamics on vegetated foreshores at sea dikes. J. Waterw. Port Coast. Ocean Eng. 147 (6), 04021035. http://dx.doi.org/10.1061/(ASCE)WW.1943-5460.0000667.

Kobayashi, N., Raichle, A.W., Asano, T., 1993. Wave attenuation by vegetation. J. Waterw. Port Coast. Ocean Eng. 119 (1), 30–48. http://dx.doi.org/10.1061/(ASCE)0733-950X(1993)119:1(30).

Kochanowski, C.A., Kastens, M., 2022. Simulation and validation of ship induced waves in shallow and confined water. In: Proceedings of 6th MASHCON, Glasgow, UK.

Krautwald, C., Von Häfen, H., Niebuhr, P., Vögele, K., Schürenkamp, D., Sieder, M., Goseberg, N., 2022. Large-scale physical modeling of broken solitary waves impacting Elevated Coastal structures. Coast. Eng. J. 64 (1), 169–189. http://dx.doi.org/10.1080/21664250.2021.2023380.

LeVeque, R.J., George, D.L., Berger, M.J., 2011. Tsunami modelling with adaptively refined finite volume methods. Acta Numer. 20, 211–289. http://dx.doi.org/10.1017/S0962492911000043.

Ma, G., Kirby, J.T., Su, S.-F., Figlus, J., Shi, F., 2013. Numerical study of turbulence and wave damping induced by vegetation canopies. Coast. Eng. 80, 68–78. http://dx.doi.org/10.1016/j.coastaleng.2013.05.007.

Martin, T., Kamath, A., Bihs, H., 2020. Modeling and simulation of Moored-floating structures using the tension element method. J. Offshore Mech. Arct. Eng. 142 (1), 011803. http://dx.doi.org/10.1115/1.4044289.

Martin, T., Tsarau, A., Bihs, H., 2021. A numerical framework for modelling the dynamics of open ocean aquaculture structures in viscous fluids. Appl. Ocean Res. 106, 102410. http://dx.doi.org/10.1016/j.apor.2020.102410.

Massel, S., Gourlay, M., 2000. On the modelling of wave breaking and set-up on coral reefs. Coast. Eng. 39 (1), 1–27. http://dx.doi.org/10.1016/S0378-3839(99)00052-6.

Mata, M.I., Van Gent, M.R., 2023. Numerical modelling of wave overtopping discharges at rubble mound breakwaters using OpenFOAM®. Coast. Eng. 181, 104274. http://dx.doi.org/10.1016/j.coastaleng.2022.104274.

Mehrtens, B., Lojek, O., Kosmalla, V., Bölker, T., Goseberg, N., 2023. Foredune growth and storm surge protection potential at the Eiderstedt Peninsula, Germany. Front. Mar. Sci. 9, 1020351. http://dx.doi.org/10.3389/fmars.2022.1020351.

Melling, G., Jansch, H., Kondziella, B., Uliczka, K., Gätje, B., 2019. Damage to rock groynes from long-period ship waves: towards a probabilistic design method. In: Proceedings of the Coastal Structures Conference 2019, Hannover, Germany. Bundesanstalt für Wasserbau, http://dx.doi.org/10.18451/978-3-939230-64-9_002.

Melling, G., Jansch, H., Kondziella, B., Uliczka, K., Gätje, B., 2020. Evaluation of optimised groyne designs in response to long-period ship wave loads at juelssand in the lower Elbe Estuary. Die Küste 89, 28. http://dx.doi.org/10.18171/1.089103.

Mintgen, F., Manhart, M., 2018. A bi-directional coupling of 2D shallow water and 3D Reynolds-averaged Navier–Stokes models. J. Hydraul. Res. 56 (6), 771–785. http://dx.doi.org/10.1080/00221686.2017.1419989.

Miquel, A., Kamath, A., Alagan Chella, M., Archetti, R., Bihs, H., 2018. Analysis of different methods for wave generation and absorption in a CFD-based numerical wave tank. J. Mar. Sci. Eng. 6 (2), 73. http://dx.doi.org/10.3390/jmse6020073.

Moideen, R., Ranjan Behera, M., Kamath, A., Bihs, H., 2019. Effect of girder spacing and depth on the solitary wave impact on coastal bridge deck for different airgaps. J. Mar. Sci. Eng. 7 (5), 140. http://dx.doi.org/10.3390/jmse7050140.

Muscalus, A.C., Haas, K.A., 2022. Vessel wake contributions to erosion at exposed and sheltered shorelines near a tidal shipping channel. Coast. Eng. 104220. http://dx.doi.org/10.1016/j.coastaleng.2022.104220.

Naot, D., Rodi, W., 1982. Calculation of secondary currents in channel flow. J. Hydraul. Eng. 108, 948–968.

Parnell, K.E., Soomere, T., Zaggia, L., Rodin, A., Lorenzetti, G., Rapaglia, J., Scarpa, G.M., 2015. Ship-induced solitary Riemann waves of depression in venice lagoon. Phys. Lett. A 379 (6), 555–559. http://dx.doi.org/10.1016/j.physleta.2014.12.004.

Paulsen, B.T., Bredmose, H., Bingham, H.B., 2014. An efficient domain decomposition strategy for wave loads on surface piercing circular cylinders. Coast. Eng. 86, 57–76. http://dx.doi.org/10.1016/j.coastaleng.2014.01.006.

Rodin, A., Soomere, T., Parnell, K.E., Zaggia, L., 2015. Numerical simulation of the propagation of ship-induced Riemann waves of depression into the Venice Lagoon. Proc. Estonian Acad. Sci. 64 (1), 22. http://dx.doi.org/10.3176/proc.2015.1.04.

Samaras, A.G., Karambas, T.V., 2021. Numerical simulation of ship-Borne waves using a 2DH post-Boussinesq model. Appl. Math. Model. 89, 1547–1556. http://dx.doi.org/10.1016/j.apm.2020.08.034.

Schweiger, C., Kaehler, C., Koldrack, N., Schuettrumpf, H., 2020. Spatial and temporal evaluation of storm-induced erosion modelling based on a two-dimensional field case including an artificial unvegetated research dune. Coast. Eng. 161, 103752. http://dx.doi.org/10.1016/j.coastaleng.2020.103752.

Terziev, M., Tezdogan, T., Oguz, E., Gourlay, T., Demirel, Y.K., Incecik, A., 2018. Numerical investigation of the behaviour and performance of ships advancing through restricted shallow waters. J. Fluids Struct. 76, 185–215. http://dx.doi.org/10.1016/j.jfluidstructs.2017.10.003.

Umesh, P., Behera, M.R., 2021. On the improvements in nearshore wave height predictions using nested SWAN-SWASH modelling in the Eastern Coastal waters of India. Ocean Eng. 236, 109550. http://dx.doi.org/10.1016/j.oceaneng.2021.109550.

Van Veelen, T.J., Fairchild, T.P., Reeve, D.E., Karunarathna, H., 2020. Experimental study on vegetation flexibility as control parameter for wave damping and velocity structure. Coast. Eng. 157, 103648. http://dx.doi.org/10.1016/j.coastaleng.2020.103648.

Vukčević, V., Jasak, H., Malenica, Š., 2016. Decomposition model for naval hydrodynamic applications, Part I: computational method. Ocean Eng. 121, 37–46. http://dx.doi.org/10.1016/j.oceaneng.2016.05.022.

Wang, W., Kamath, A., Martin, T., Pákozdi, C., Bihs, H., 2020a. A comparison of different wave modelling techniques in an open-source hydrodynamic framework. J. Mar. Sci. Eng. 8 (7), 526. http://dx.doi.org/10.3390/jmse8070526.

Wang, W., Martin, T., Kamath, A., Bihs, H., 2020b. An improved depth-averaged non-hydrostatic shallow water model with quadratic pressure approximation. Internat. J. Numer. Methods Fluids 92 (8), 803–824. http://dx.doi.org/10.1002/fld.4807.

Wang, W., Pákozdi, C., Kamath, A., Martin, T., Bihs, H., 2022. Hydrodynamic coupling of viscous and nonviscous numerical wave solutions within the open-source hydrodynamics framework REEF3D. J. Offshore Mech. Arct. Eng. 144 (4), 041903. http://dx.doi.org/10.1115/1.4053848.

Windt, C., Davidson, J., Schmitt, P., Ringwood, J., 2019. On the assessment of numerical wave makers in CFD simulations. J. Mar. Sci. Eng. 7 (2), 47. http://dx.doi.org/10.3390/jmse7020047.

Zhou, H., Moore, C.W., Wei, Y., Titov, V.V., 2011. A nested-grid Boussinesq-type approach to modelling dispersive propagation and runup of landslide-generated tsunamis. Nat. Hazards Earth Syst. Sci. 11 (10), 2677–2697. http://dx.doi.org/10.5194/nhess-11-2677-2011.

Further reading

Windt, C., Untrau, A., Davidson, J., Ransley, E.J., Greaves, D.M., Ringwood, J.V., 2021. Assessing the validity of regular wave theory in a short physical wave flume using particle image velocimetry. Exp. Therm Fluid Sci. 121, 110276. http://dx.doi.org/10.1016/j.expthermflusci.2020.110276.